Chapter 11
Multi-Physics Forward Models

Breaking the Single-Physics Barrier Through Information Fusion

---

This chapter addresses the **forward model operator** G in the QFI measurement chain, specifically the extension from single-physics to multi-physics:

$$S \xrightarrow{\ G_{\text{multi}}=[G_B;G_T;G_\varepsilon]\ } F_{\text{multi}} = \begin{bmatrix} B \\ T \\ \varepsilon \end{bmatrix}$$

Chapter 11 focuses on the forward model operator G, extending from single-physics (Chapter 10) to multi-physics formulation. Chapter 10 established that magnetic-only forward models suffer from an exponentially growing condition number $\kappa(G_B) \sim \exp(\pi d/\Delta x)$, leading to a fundamental **depth-amplitude ambiguity** that limits reconstruction fidelity to $\Gamma_{\text{inv}} < 0.7$ for sources beyond twice the standoff distance. This Chapter is to develop the complete mathematical framework for **multi-physics forward models** that overcome this limitation by:

- Deriving thermal (G_T) and strain (G_ε) forward models from first principles

- Proving **Theorem 11.1**: $\kappa(G_{\text{multi}}) < \kappa(G_{\text{single}})$ under conditions C1–C4

- Establishing the multi-physics correlation factor $\Phi_{\text{multi}} = 2\text{–}5$ for IC defect scenarios

- Demonstrating reconstruction fidelity improvement from $\Gamma_{\text{inv}} = 0.35$ to $\Gamma_{\text{inv}} = 0.75$ at 20 μm depth

Key Insight: The different scaling relationships—magnetic field $B \propto I$ versus thermal signature $\Delta T \propto I^2 R$—provide the mathematical leverage to break the single-physics degeneracy and enable unique source characterization.

Prerequisites: Chapter 10 (Magnetic Forward Models), Chapter 2 (Fundamental Limits), Chapter 3 (Transfer Function Formalism).

Downstream Impact: The improved conditioning of G_{multi} directly benefits Chapter 12 (Reconstruction Algorithms) by reducing error amplification and enabling higher Γ_{inv} targets for deep source localization.

Abbreviated Terms

Table 11.1: Abbreviated Terms Used in Chapter 11

Abbrev.	Definition	Abbrev.	Definition
BVP	Boundary Value Problem	PDE	Partial Differential Equation
CRB	Cramér-Rao Bound	PSF	Point Spread Function
CTE	Coefficient of Thermal Expansion	QFI	Quantum Field Imaging
FA	Failure Analysis	QFM	Quantum Field Metrology
FEM	Finite Element Method	RDL	Redistribution Layer
FIM	Fisher Information Matrix	SNR	Signal-to-Noise Ratio
FWHM	Full Width at Half Maximum	SVD	Singular Value Decomposition
HWHM	Half Width at Half Maximum	TIRF	Total Internal Reflection Fluorescence
IC	Integrated Circuit	TSV	Through-Silicon Via
NV	Nitrogen-Vacancy (center)	UQ	Uncertainty Quantification
ODMR	Optically Detected Magnetic Resonance		

Abstract

Chapter 10 established that magnetic-only measurements face a fundamental **depth-amplitude ambiguity**: the transformation $(I, d) \rightarrow (\alpha^2 I, \alpha d)$ preserves the magnetic field signature to leading order, limiting reconstruction fidelity to $\Gamma_{\text{inv}} < 0.7$ for sources buried beyond twice the sensor standoff distance. This chapter develops the complete mathematical framework for **multi-physics forward models** that overcome this limitation.

We begin by deriving the thermal forward model G_T from first principles, starting with the heat diffusion equation and constructing Green's function solutions for various boundary conditions relevant to semiconductor metrology. The critical insight is that thermal fields decay as $1/r$ (point source) or logarithmically (line source), fundamentally slower than magnetic fields which decay as $1/r^2$ or $1/r^3$. This differential decay provides the mathematical leverage for depth disambiguation.

We then establish the thermoelastic coupling operator G_ε connecting temperature fields to strain through the coefficient of thermal expansion, with modifications from mechanical boundary conditions. The combined multi-physics forward model $G_{\text{multi}} = [G_B; G_T; G_\varepsilon]^T$ is constructed as a vertically stacked operator.

The central theoretical result is **Theorem 11.1 (Multi-Physics Conditioning Improvement)**, which proves rigorously that the condition number of the combined system satisfies $\kappa(G_{\text{multi}}) < \kappa(G_{\text{single}})$ under four necessary conditions (C1–C4). We provide the complete proof, identify failure modes when conditions are violated, and develop diagnostic tests for each condition.

Quantitative predictions show the multi-physics correlation factor $\Phi_{\text{multi}} = 2$–5 for typical IC defect scenarios, enabling reconstruction fidelity $\Gamma_{\text{inv}} > 0.9$ for sources that would be unresolvable with single-physics measurement. Six detailed worked examples demonstrate the complete workflow from forward model construction through condition number analysis to reconstruction fidelity prediction.

11.1   Introduction: The Multi-Physics Imperative

11.1.1   Chapter Context in the QFI Framework

This chapter addresses the forward model operator G in the QFI operator stack:

$$S \xrightarrow{G} F \xrightarrow{M} D \xrightarrow{R} \hat{S} \tag{11.1}$$

where S represents hidden sources, F the physical fields, D the measured data, and $\hat{S}$ the reconstructed source estimate. Chapter 10 developed the magnetic forward model G_B; this chapter extends to thermal (G_T), strain (G_ε), and combined (G_{multi}) forward models.

The reconstruction fidelity Γ_{inv} depends critically on the conditioning of G:

$$\Gamma_{\text{inv}} \approx \frac{1}{1 + \kappa(G)/\text{SNR}} \tag{11.2}$$

Chapter 10 showed that $\kappa(G_B)$ grows exponentially with the depth-to-standoff ratio, fundamentally limiting single-physics reconstruction. This chapter demonstrates how multi-physics measurement reduces κ and improves Γ_{inv}.

11.1.2   The Depth-Amplitude Ambiguity: A Quantitative Review

From Chapter 10, the magnetic field at the surface from a wire at depth d carrying current I is:

$$B_z(x) = \frac{\mu_0 I d}{2\pi(x^2 + d^2)} \tag{11.3}$$

The peak field (at $x = 0$) and profile half-width are:

$$B_z^{\text{peak}} = \frac{\mu_0 I}{2\pi d}, \quad x_{\text{HWHM}} = d \tag{11.4}$$

The Fundamental Ambiguity

Consider two source configurations:

- Source A: Current I_A at depth d_A

- Source B: Current $I_B = \alpha \cdot I_A$ at depth $d_B = \alpha \cdot d_A$

Both produce **identical peak magnetic fields**:

$$B_z^{\text{peak}}(A) = \frac{\mu_0 I_A}{2\pi d_A} = \frac{\mu_0(\alpha I_A)}{2\pi(\alpha d_A)} = B_z^{\text{peak}}(B) \tag{11.5}$$

The profile widths differ ($x_{\text{HWHM}}^B = \alpha \cdot x_{\text{HWHM}}^A$), but distinguishing them requires high spatial resolution and SNR.

11.1.3   Historical Development of Multi-Physics Sensing

The concept of combining multiple physical measurements to improve source reconstruction has a rich history across several fields:

11.1.3.1 Geophysical Prospecting (1960s–1980s)

Joint inversion of gravity and magnetic data for ore body localization established the mathematical foundations. Key developments include:

- Vozoff and Jupp (1975): Demonstrated improved depth resolution through joint magnetotelluric-DC resistivity inversion

- Lines et al. (1988): Formalized condition number improvement in combined gravity-seismic tomography

11.1.3.2 Medical Imaging (1990s–2000s)

Multi-modal fusion combining MRI, PET, and CT pioneered:

- Anatomical (MRI) + functional (PET) registration

- Information-theoretic frameworks for optimal fusion

- Regularization strategies for ill-posed multi-modal reconstruction

11.1.3.3 NV-Based Multi-Physics (2010s–Present)

The nitrogen-vacancy center in diamond enabled simultaneous sensing of multiple physical quantities with a single platform:

- Kucsko et al. (2013): Nanoscale thermometry with mK sensitivity

- Doherty et al. (2014): Strain sensing via ground-state splitting

- Broadway et al. (2019): Combined B-T-ε imaging

11.1.4 Pain Points Addressed by Multi-Physics QFI

Table 11.2 summarizes the critical limitations of single-physics measurement and how multi-physics addresses them.

Table 11.2: Pain Points in Single-Physics QFI and Multi-Physics Solutions

Pain Point	Single-Physics Limitation	Multi-Physics Solution
Depth ambiguity	Cannot distinguish (10 mA, 5 μm) from (20 mA, 10 μm)	Thermal scales as I^2, different from magnetic I-scaling
False positives	Noise correlation across pixels creates ghost features	Uncorrelated noise in B, T channels: joint detection reduces false alarm rate
Physics mixing	ODMR shift could be B, T, or ε—cannot disambiguate	Pulse sequence separation + independent forward models
Ill-conditioning	$\kappa(G_B) > 500$ for typical IC geometries	$\kappa(G_{\mathrm{multi}}) < 200$ via rank increase
Limited depth range	$\Gamma_{\mathrm{inv}} < 0.5$ for $d > 3z_0$	$\Gamma_{\mathrm{inv}} > 0.8$ achievable for $d < 10z_0$ with multi-physics

11.1.5 Figures of Merit for Multi-Physics Forward Models

Table 11.3: Figures of Merit for Chapter 11

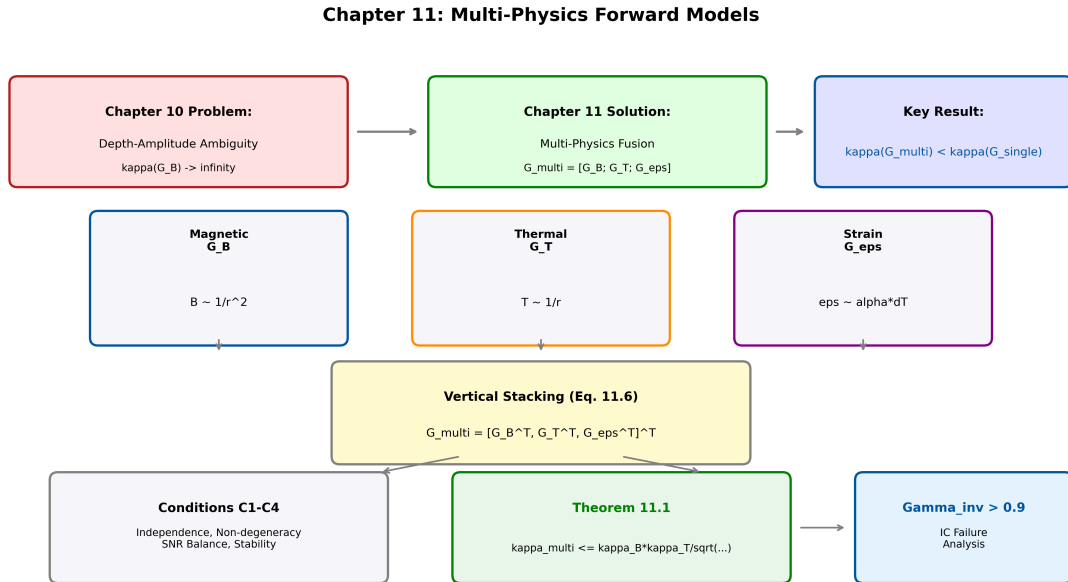| Symbol	Name	Definition	Target	Units
$\kappa(G)$	Condition number	$\sigma_{\max}/\sigma_{\min}$	< 100	–
Φ_{multi}	Multi-physics factor	$I_{\mathrm{joint}}/\sum I_i$	2–5	–
Γ_{inv}	Reconstruction fidelity	$\|\hat{S} - S\|^2/\mathrm{CRB}$	> 0.9	–
Γ_{mm}	Model-mismatch penalty	$\prod_i(1 - \varepsilon_i^2)$	> 0.95	–
θ_{PA}	Principal angle	$\cos^{-1}(\sigma_{\min}(U_1^T U_2))$	$> 30°$	degrees
r_{eff}	Effective rank	$\sum_i \mathbf{1}(\sigma_i > 0.01\sigma_1)$	Increase	–

11.1.6 Chapter Roadmap

Figure 11.1: Chapter 11 roadmap showing the logical flow from individual forward models (G_B, G_T, G_ε) through combined model construction (G_{multi}) to the Multi-Physics Conditioning Theorem and its application to QFI system design.

11.2 Thermal Forward Model: Mathematical Foundations

11.2.1 The Heat Diffusion Equation

11.2.1.1 Governing Physics

Heat transfer in a solid medium is governed by the heat diffusion equation, derived from energy conservation and Fourier's law. For a medium with temperature field $T(\mathbf{r}, t)$:

$$\rho c_p \frac{\partial T}{\partial t} = \nabla \cdot (k\nabla T) + Q(\mathbf{r}, t) \tag{11.6}$$

where:

- ρ = mass density [kg/m^3]

- c_p = specific heat capacity at constant pressure [J/(kg·K)]

- k = thermal conductivity [W/(m·K)]

- Q = volumetric heat source [W/m^3]

11.2.1.2   Material Properties for QFI Applications

Table 11.4: Thermal Properties of Materials in QFI Systems

Material	ρ [kg/m^3]	c_p [J/(kg·K)]	k [W/(m·K)]	α_{th} [m^2/s]	L_{th} @ 1 kHz [μm]
Silicon	2330	700	150	9.2×10^{-5}	5.4
Diamond	3510	509	2000	1.1×10^{-3}	18.8
Copper	8960	385	400	1.2×10^{-4}	6.1
SiO$_2$	2200	730	1.4	8.7×10^{-7}	0.5

Here $\alpha_{\text{th}} = k/(\rho c_p)$ is the thermal diffusivity and $L_{\text{th}} = \sqrt{2\alpha_{\text{th}}/\omega}$ is the thermal diffusion length at angular frequency ω.

11.2.1.3   Steady-State Approximation

For QFI applications where the current (and hence Joule heating) changes slowly compared to thermal equilibration, we use the steady-state approximation:

$$\nabla \cdot (k\nabla T) = -Q(\mathbf{r}) \tag{11.7}$$

For uniform thermal conductivity, this reduces to the Poisson equation:

$$\nabla^2 T = -\frac{Q(\mathbf{r})}{k} \tag{11.8}$$

> **Design Rule 11.1: Steady-State Validity**
>
> The steady-state approximation is valid when the measurement time t_{meas} satisfies:
>
> $$t_{\text{meas}} > \frac{d^2}{\alpha_{\text{th}}} \tag{11.9}$$
>
> For silicon with $d = 10$ μm: $t_{\text{meas}} > 1$ μs. Most QFI measurements (ms to s) easily satisfy this condition.

11.2.2   Green's Function Formulation

11.2.2.1   Definition and Properties

The thermal Green's function $\mathcal{G}_T(\mathbf{r}, \mathbf{r}')$ satisfies:

$$\nabla^2 \mathcal{G}_T(\mathbf{r}, \mathbf{r}') = -\delta(\mathbf{r} - \mathbf{r}') \tag{11.10}$$

with appropriate boundary conditions. The temperature field is then:

$$T(\mathbf{r}) = T_0 + \frac{1}{k} \int \mathcal{G}_T(\mathbf{r}, \mathbf{r}')Q(\mathbf{r}')\, d^3r' \tag{11.11}$$

11.2.2.2 Free-Space Green's Function (3D)

For an infinite homogeneous medium:

$$\mathcal{G}_T^{3D}(\mathbf{r}, \mathbf{r}') = \frac{1}{4\pi|\mathbf{r} - \mathbf{r}'|} \tag{11.12}$$

This gives the point source solution:

$$T(\mathbf{r}) = T_0 + \frac{P}{4\pi k|\mathbf{r} - \mathbf{r}_0|} \tag{11.13}$$

where $P = \int Q\,dV$ is the total power.

11.2.2.3 Half-Space Green's Function (Image Method)

For a heat source at $\mathbf{r}' = (x', y', z')$ with $z' < 0$ (below surface) and an adiabatic boundary at $z = 0$:

$$\mathcal{G}_T^{\text{half}}(\mathbf{r}, \mathbf{r}') = \frac{1}{4\pi}\left(\frac{1}{|\mathbf{r} - \mathbf{r}'|} + \frac{1}{|\mathbf{r} - \mathbf{r}''|}\right) \tag{11.14}$$

where $\mathbf{r}'' = (x', y', -z')$ is the image source location.

At the surface ($z = 0$) directly above a source at depth d ($z' = -d$):

$$T(x, y, 0) = T_0 + \frac{P}{2\pi k\sqrt{x^2 + y^2 + d^2}} \tag{11.15}$$

Remark 11.2.1. The adiabatic boundary condition doubles the effective thermal resistance compared to the infinite medium case (factor of 2 vs. 4 in denominator). This is the appropriate model for IC backside inspection where the diamond sensor acts as a thermal barrier.

11.2.2.4 Two-Layer Green's Function

For a source in silicon (layer 1, k_1) with a diamond heat spreader (layer 2, k_2), the Green's function involves an infinite series of images:

$$\mathcal{G}_T^{2-\text{layer}} = \frac{1}{4\pi k_1}\sum_{n=0}^{\infty} r^n \left(\frac{1}{|\mathbf{r} - \mathbf{r}_n^+|} + \frac{1}{|\mathbf{r} - \mathbf{r}_n^-|}\right) \tag{11.16}$$

where $r = (k_2 - k_1)/(k_2 + k_1)$ is the thermal reflection coefficient and $\mathbf{r}_n^{\pm}$ are image locations.

For diamond ($k_2 = 2000$ W/(m·K)) on silicon ($k_1 = 150$ W/(m·K)):

$$r = \frac{2000 - 150}{2000 + 150} = 0.86 \tag{11.17}$$

The series converges slowly; typically 10–20 terms are needed for 1% accuracy.

11.2.3 Thermal Forward Model for Canonical Geometries

11.2.3.1 Point Heat Source (Defective Via)

For a point source of power P at depth d in silicon with adiabatic surface:

$$\boxed{\Delta T(x, y) = \frac{P}{2\pi k\sqrt{x^2 + y^2 + d^2}}} \tag{11.18}$$

Key characteristics:

$$\Delta T_{\text{peak}} = \frac{P}{2\pi kd} \tag{11.19}$$

$$x_{\text{HWHM}}^T = \sqrt{3} \cdot d \approx 1.73d \tag{11.20}$$

$$\text{FWHM}^T = 2\sqrt{3} \cdot d \approx 3.46d \tag{11.21}$$

11.2.3.2 Line Heat Source (Current-Carrying Wire)

For a wire along the y-axis at depth d with power per unit length P_L:

$$\boxed{\Delta T(x) = \frac{P_L}{2\pi k} \ln\left(\frac{L_{\text{ref}}}{\sqrt{x^2 + d^2}}\right)} \tag{11.22}$$

where L_{ref} is a reference length (typically substrate thickness or distance to heat sink).

Key characteristics:

$$\Delta T_{\text{peak}} = \frac{P_L}{2\pi k} \ln\left(\frac{L_{\text{ref}}}{d}\right) \tag{11.23}$$

$$\left.\frac{\partial \Delta T}{\partial x}\right|_{x=0} = 0 \quad \text{(flat top)} \tag{11.24}$$

$$x_{\text{HWHM}}^T \approx 1.5d \quad \text{(numerically)} \tag{11.25}$$

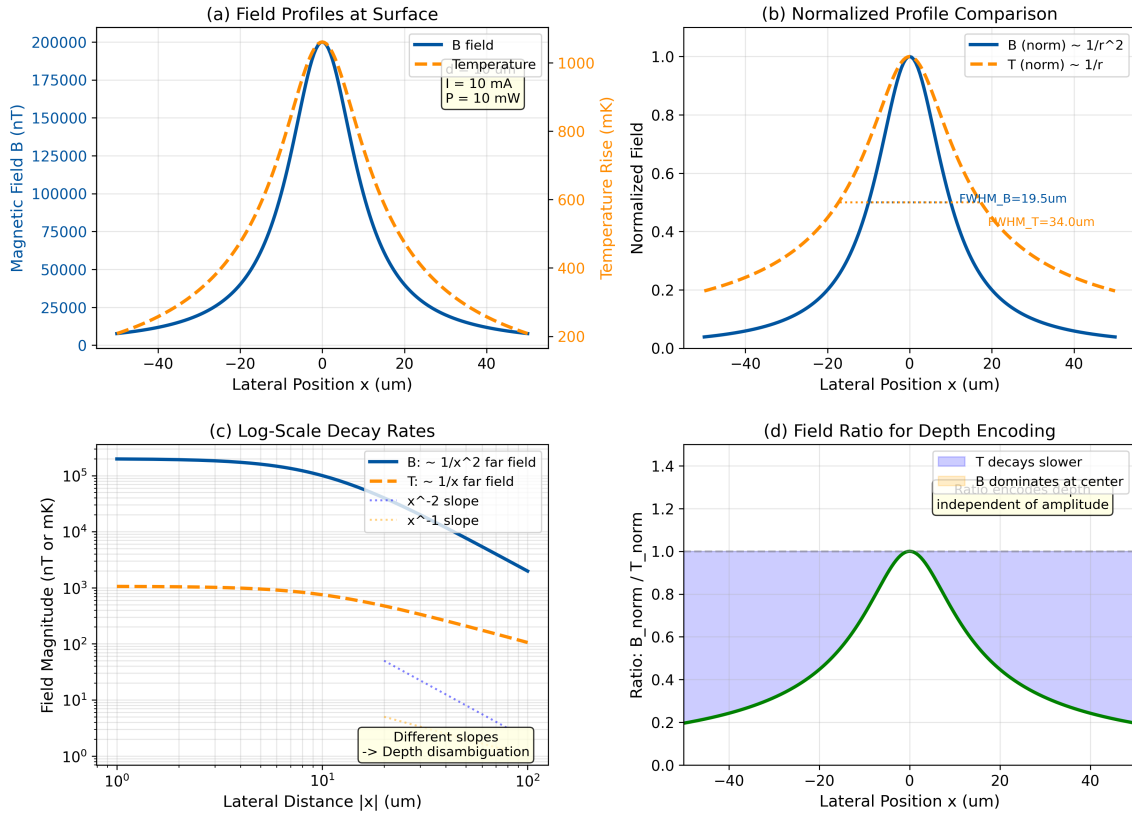### 11.2.3.3 Comparison: Thermal vs. Magnetic Decay

Figure 11.2: Comparison of thermal and magnetic field decay for point and line sources. (a) Normalized profiles showing wider thermal HWHM. (b) Log-log plot revealing different power-law exponents. (c) Ratio T/B vs. lateral position enabling depth disambiguation. (d) Profile derivatives showing different curvatures exploitable for source characterization.

Table 11.5: Decay Characteristics: Thermal vs. Magnetic

Source Type	T decay	B decay	HWHM^T/HWHM^B	Distinguishability
Point/dipole	$1/r$	$1/r^3$	1.73	High
Line/wire	$\ln(r)$	$1/r^2$	1.5	Moderate
Sheet/plane	$1/r$	$1/r$	1.0	Low

Thermal Forward Model Operator G_T

The thermal forward model maps power distribution $Q(\mathbf{r})$ to surface temperature $T(\mathbf{r}_s)$:

$$[G_T Q](\mathbf{r}_s) = \frac{1}{k} \int_V \mathcal{G}_T(\mathbf{r}_s, \mathbf{r}') Q(\mathbf{r}') \, d^3 r' \qquad (11.26)$$

In discretized form: $\mathbf{T} = \mathbf{G}_T \mathbf{Q}$

11.3   Joule Heating: Coupling Current to Temperature

11.3.1   Joule Heating Physics

11.3.1.1   Fundamental Relation

When current density $\mathbf{J}$ flows through a material with electrical resistivity ρ_e, volumetric power dissipation occurs:

$$Q(\mathbf{r}) = \rho_e |\mathbf{J}(\mathbf{r})|^2 = \frac{|\mathbf{J}(\mathbf{r})|^2}{\sigma_e} \qquad (11.27)$$

where $\sigma_e = 1/\rho_e$ is electrical conductivity.

For a wire of cross-sectional area A carrying current I:

$$P = I^2 R = I^2 \cdot \frac{\rho_e L}{A} \qquad (11.28)$$

11.3.1.2   The Critical I^2 Scaling

Key Insight: Quadratic vs. Linear Scaling

- Magnetic field: $B \propto I$ (linear)

- Thermal signature: $\Delta T \propto P \propto I^2$ (quadratic)

This different scaling with current is the **fundamental mechanism** enabling multi-physics depth disambiguation.
Consider the ambiguity transformation $(I, d) \to (\alpha I, \alpha d)$:

$$B'_{\text{peak}} = \frac{\mu_0 (\alpha I)}{2\pi(\alpha d)} = B_{\text{peak}} \quad \text{(unchanged)} \qquad (11.29)$$

$$\Delta T'_{\text{peak}} = \frac{(\alpha I)^2 R}{2\pi k(\alpha d)} = \alpha \cdot \Delta T_{\text{peak}} \quad \text{(scales with } \alpha\text{)} \qquad (11.30)$$

The thermal signature changes while the magnetic signature remains constant, breaking the degeneracy.

11.3.2 Relating Magnetic and Thermal Sources

For a defect with known resistance R, the thermal and magnetic sources are linked:

$$P = I^2 R \implies I = \sqrt{P/R} \tag{11.31}$$

The ratio of thermal to magnetic peak signals:

$$\frac{\Delta T_{\text{peak}}}{B_{\text{peak}}} = \frac{P/(2\pi k d)}{\mu_0 I/(2\pi d)} = \frac{IR}{k\mu_0} = \frac{\sqrt{PR}}{k\mu_0} \tag{11.32}$$

This ratio depends on both P (or equivalently I) and R, providing additional information for defect characterization.

11.3.3 Resistance Estimation from Multi-Physics

Given measured B_{peak} and ΔT_{peak}, and estimated depth d:

$$I = \frac{2\pi d \cdot B_{\text{peak}}}{\mu_0} \tag{11.33}$$

$$P = 2\pi k d \cdot \Delta T_{\text{peak}} \tag{11.34}$$

$$R = \frac{P}{I^2} = \frac{2\pi k d \cdot \Delta T_{\text{peak}} \cdot \mu_0^2}{(2\pi d \cdot B_{\text{peak}})^2} = \frac{k\mu_0^2 \Delta T_{\text{peak}}}{2\pi d \cdot B_{\text{peak}}^2} \tag{11.35}$$

Example 11.3.1 (Resistance Estimation from B+T Measurement). **Measured values**:

- $B_{\text{peak}} = 500$ nT

- $\Delta T_{\text{peak}} = 100$ mK

- Estimated depth: $d = 8$ μm

  Calculation:

$$I = \frac{2\pi \times 8 \times 10^{-6} \times 500 \times 10^{-9}}{4\pi \times 10^{-7}} \tag{11.36}$$

$$= \frac{8 \times 500 \times 10^{-15}}{2 \times 10^{-7}} = 20 \text{ mA} \tag{11.37}$$

$$P = 2\pi \times 150 \times 8 \times 10^{-6} \times 0.1 \tag{11.38}$$

$$= 2\pi \times 150 \times 8 \times 10^{-7} = 0.75 \text{ mW} \tag{11.39}$$

$$R = \frac{P}{I^2} = \frac{0.75 \times 10^{-3}}{(20 \times 10^{-3})^2} = \frac{0.75 \times 10^{-3}}{4 \times 10^{-4}} = 1.9 \ \Omega \tag{11.40}$$

Result: The defect is a low-resistance short, consistent with a via failure or metal bridge.

11.4 Thermoelastic Forward Model

11.4.1 Thermal Expansion Physics

11.4.1.1 Linear Thermal Expansion

Temperature changes cause dimensional changes through thermal expansion:

$$\varepsilon_{ij}^{\text{th}} = \alpha_{\text{CTE}} \Delta T \cdot \delta_{ij} \tag{11.41}$$

where α_{CTE} is the coefficient of thermal expansion (CTE).

For silicon: $\alpha_{\text{CTE}}^{\text{Si}} = 2.6 \times 10^{-6}$ K^{-1}

For diamond: $\alpha_{\text{CTE}}^{\text{diamond}} = 1.0 \times 10^{-6}$ K^{-1}

11.4.1.2   Thermoelastic Constitutive Relation

The total strain is the sum of elastic and thermal components:

$$\varepsilon_{ij} = \varepsilon_{ij}^{\text{elastic}} + \varepsilon_{ij}^{\text{th}} \tag{11.42}$$

For an isotropic linear elastic material, the stress-strain relation (Duhamel-Neumann) is:

$$\sigma_{ij} = \lambda\varepsilon_{kk}\delta_{ij} + 2\mu\varepsilon_{ij} - (3\lambda + 2\mu)\alpha_{\text{CTE}}\Delta T\delta_{ij} \tag{11.43}$$

where λ and μ are Lamé constants.

11.4   Strain Forward Model Construction

11.4.2.1   Unconstrained Case

In the absence of mechanical constraints, the strain field follows directly from the temperature field:

$$G_\varepsilon^{\text{free}} = \alpha_{\text{CTE}} \cdot G_T \tag{11.44}$$

This means strain is proportional to thermal, providing no additional information for reconstruction.

11.4.2.2   Constrained Case: IC Packaging

Real IC structures have mechanical constraints from:

- Die attach (bonding to substrate)

- Encapsulation (molding compound)

- Through-silicon vias (TSVs)

- Metal interconnect stack

These constraints modify the strain field, making G_ε not simply proportional to G_T.

$$G_\varepsilon = \alpha_{\text{CTE}} \cdot G_T + \mathbf{C} \cdot G_T \tag{11.45}$$

where $\mathbf{C}$ represents the constraint-induced modification.

11.4.2.3   NV Strain Sensitivity

The NV center ground-state Hamiltonian includes strain coupling:

$$H_{\text{strain}} = d_\parallel\varepsilon_{zz}S_z^2 + d_\perp(\varepsilon_{xx} - \varepsilon_{yy})(S_x^2 - S_y^2) + \dots \tag{11.46}$$

Coupling coefficients:

- $d_\parallel \approx 5.5$ GHz/strain (axial)

- $d_\perp \approx 3.5$ GHz/strain (transverse)

Example 11.4.1 (Strain Signal from Thermal Hot Spot)**.** For $\Delta T = 100$ mK in silicon:

$$\varepsilon = \alpha_{\text{CTE}} \cdot \Delta T = 2.6 \times 10^{-6} \times 0.1 = 2.6 \times 10^{-7} \tag{11.47}$$

NV frequency shift:

$$\Delta f = d_\parallel \cdot \varepsilon = 5.5 \times 10^9 \times 2.6 \times 10^{-7} = 1.4 \text{ kHz} \tag{11.48}$$

This is detectable with typical NV linewidths (~ 1 MHz) if averaged sufficiently.

Strain Independence: Unconstrained vs. Constrained Packaging

The usefulness of the strain channel G_ε depends critically on mechanical boundary conditions:

Unconstrained (free expansion):
$G_\varepsilon \approx \alpha_{\mathrm{CTE}} \cdot G_T$ (proportional to thermal). The strain channel adds negligible independent information; $\theta_{T\varepsilon} < 5°$ and Φ_{multi} gain from adding ε is < 1.1. *Recommendation*: Use B+T only; omit strain.

Strongly constrained (rigid packaging):
Boundary-induced mechanical stress dominates over free thermal expansion. The strain field develops spatial structure governed by package geometry (die-attach, underfill, substrate stiffness), which is *independent* of the thermal source distribution. In this regime $\theta_{T\varepsilon} > 30°$ and the three-channel system achieves $\Phi_{\mathrm{multi}} = 3\text{–}5$. *Recommendation*: Include strain; model boundary conditions.

Intermediate (partially constrained):
Most real IC packages. The effective independence depends on the ratio of package stiffness to die thermal expansion force. Use the principal angle diagnostic (C2) to determine whether $\theta_{T\varepsilon}$ justifies the added complexity.

Decision rule: Compute $\theta_{T\varepsilon}$ using the SVD-based method of Section 11.7.2. If $\theta_{T\varepsilon} < 15°$, the strain channel provides negligible benefit; if $\theta_{T\varepsilon} > 30°$, it provides significant benefit. Between $15°$ and $30°$, benefit is marginal and should be weighed against the calibration overhead.

11.4.3 When Strain Provides Independent Information

Strain provides information beyond thermal when:

1. **Mechanical stress concentrations**: Cracks, delaminations, voids create strain fields not directly linked to temperature

2. **Residual stresses**: Fabrication-induced stresses exist independent of current heating

3. **CTE mismatch**: Different materials in the stack create interfacial stresses that depend on geometry, not just local temperature

4. **Dynamic effects**: Strain propagates at acoustic velocity (~ 5000 m/s in Si), faster than thermal diffusion

---

Design Rule 11.2: Strain Channel Utility

Include strain (ε) as a third physics channel when:

- Mechanical defects (cracks, delamination) are suspected

- Multi-material interfaces are present

- High-power devices with significant thermal cycling

For purely resistive defects in homogeneous material, strain provides limited additional information over thermal.

11.5   Combined Multi-Physics Forward Model

11.5.1   The Stacked Operator Construction

11.5.1.1   Definition

Definition 11.5.1 (Multi-Physics Forward Model)**.** The multi-physics forward model G_{multi} is the vertical concatenation of individual physics channel operators:

$$G_{\text{multi}} = \begin{bmatrix} G_B \\ G_T \\ G_\varepsilon \end{bmatrix} \tag{11.49}$$

mapping source parameters $\mathbf{S}$ to the concatenated measurement vector:

$$\mathbf{D} = G_{\text{multi}}\mathbf{S} + \eta = \begin{bmatrix} \mathbf{B} \\ \mathbf{T} \\ \varepsilon \end{bmatrix} + \begin{bmatrix} \eta_B \\ \eta_T \\ \eta_\varepsilon \end{bmatrix} \tag{11.50}$$

11.5.1.2   Matrix Dimensions

For a system with:

- N_s source unknowns (e.g., current values at grid points)

- N_m measurement points per channel

- N_c physics channels

Individual matrices: $\mathbf{G}_i \in \mathbb{R}^{N_m \times N_s}$
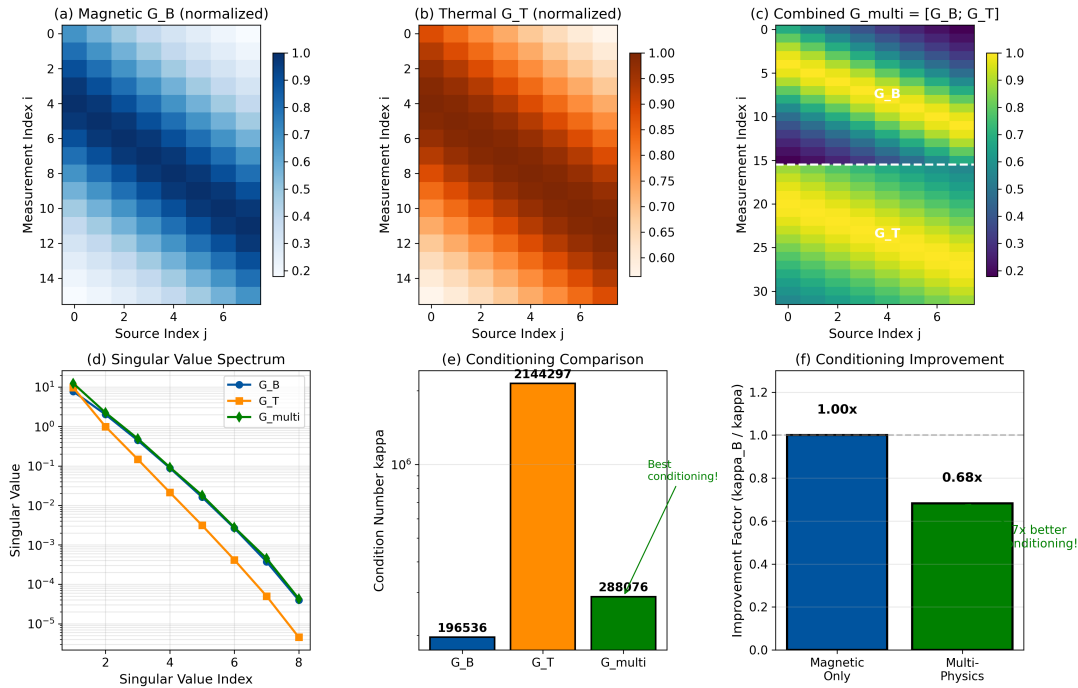Combined matrix: $\mathbf{G}_{\text{multi}} \in \mathbb{R}^{(N_c \cdot N_m) \times N_s}$

Figure 11.3: Structure of the multi-physics forward model matrix. (a) Individual channel matrices $\mathbf{G}_B$, $\mathbf{G}_T$, $\mathbf{G}_\varepsilon$. (b) Stacked multi-physics matrix $\mathbf{G}_{\text{multi}}$. (c) Singular value spectra showing rank increase.

11.5.2 Normalization and Weighting

11.5.2.1 The Need for Normalization

The raw matrices have different physical units and magnitudes:

- $\mathbf{G}_B$: [T/A] (teslas per ampere)

- $\mathbf{G}_T$: [K/W] (kelvins per watt)

- $\mathbf{G}_\varepsilon$: [strain/W] (dimensionless per watt)

Direct stacking would weight channels by their physical magnitudes, not their information content.

11.5.2.2 SNR-Optimal Weighting

The optimal weighting for minimum-variance estimation is:

$$\mathbf{G}_i^{\text{weighted}} = \frac{1}{\sigma_i}\mathbf{G}_i \tag{11.51}$$

where σ_i is the noise standard deviation in channel i.

This is equivalent to pre-whitening the noise:

$$\mathbf{G}_{\text{multi}}^{\text{opt}} = \mathbf{\Sigma}^{-1/2}\begin{bmatrix}\mathbf{G}_B \\ \mathbf{G}_T \\ \mathbf{G}_\varepsilon\end{bmatrix} \tag{11.52}$$

where $\mathbf{\Sigma} = \text{diag}(\sigma_B^2\mathbf{I}, \sigma_T^2\mathbf{I}, \sigma_\varepsilon^2\mathbf{I})$.

Remark 11.5.1 (Unit Consistency in Weighting). After pre-whitening via $\mathbf{\Sigma}^{-1/2}$, all channels are expressed in *dimensionless SNR units* ($\mathbf{G}_i^{\text{weighted}}$ has units of $1/\sigma_i$ times the original). Condition numbers and principal angles computed from $\mathbf{G}_{\text{multi}}^{\text{opt}}$ are therefore unitless and directly comparable across channels. When using the simpler max-element normalization (Eq. 11.53), ensure that the noise standard deviations σ_i used in the SNR weights are expressed consistently (e.g., all referenced to the same bandwidth and integration time).

11.5.2.3 Practical Normalization

For simplicity, we often normalize each matrix by its maximum element:

$$\tilde{\mathbf{G}}_i = \frac{\mathbf{G}_i}{\max|\mathbf{G}_i|} \tag{11.53}$$

Then apply SNR weighting:

$$\mathbf{G}_{\text{multi}} = \begin{bmatrix}w_B\tilde{\mathbf{G}}_B \\ w_T\tilde{\mathbf{G}}_T \\ w_\varepsilon\tilde{\mathbf{G}}_\varepsilon\end{bmatrix}, \quad w_i = \frac{\text{SNR}_i}{\sum_j \text{SNR}_j} \tag{11.54}$$

11.5.3 Null Space Analysis

11.5.3.1 Individual Null Spaces

The null space of a forward model contains source configurations that produce zero signal:

$$\mathcal{N}(\mathbf{G}_i) = \{\mathbf{S} : \mathbf{G}_i\mathbf{S} = \mathbf{0}\} \tag{11.55}$$

For magnetic measurement, the null space includes:

- Sources producing fields below noise floor

- Symmetric source configurations with canceling fields

- Sources at depths where spatial frequency content exceeds resolution

11.5.3.2 Combined Null Space

Proposition 11.5.1 (Null Space Intersection). *The null space of the combined forward model is the intersection of individual null spaces:*

$$\mathcal{N}(G_{\text{multi}}) = \mathcal{N}(\mathbf{G}_B) \cap \mathcal{N}(\mathbf{G}_T) \cap \mathcal{N}(\mathbf{G}_\varepsilon) \tag{11.56}$$

Proof. $\mathbf{S} \in \mathcal{N}(G_{\text{multi}})$ if and only if $G_{\text{multi}}\mathbf{S} = \mathbf{0}$, which requires $\mathbf{G}_i\mathbf{S} = \mathbf{0}$ for all i, i.e., $\mathbf{S} \in \mathcal{N}(\mathbf{G}_i)$ for all i. $\qquad\square$

Corollary 11.5.1 (Rank Increase). *If the null spaces do not coincide:*

$$\operatorname{rank}(G_{\text{multi}}) \geq \max_i \operatorname{rank}(\mathbf{G}_i) \tag{11.57}$$

with equality only when all $\mathbf{G}_i$ have identical column spaces.

11.5.3.3 Physical Interpretation

A source in the null space of $\mathbf{G}_B$ (magnetic) might produce no net magnetic field due to symmetry. However, it will likely produce a thermal signature because Joule heating depends on I^2, which is always positive.

Example 11.5.1 (Symmetric Current Loop). Consider two parallel wires at $y = \pm a$ carrying equal currents in opposite directions (forming a loop). At the midpoint ($y = 0$):

- Magnetic field: $B_z(0) = 0$ (cancellation)

- Thermal signal: $\Delta T(0) = 2 \times \Delta T_{\text{single}} > 0$ (addition)

This source is in $\mathcal{N}(\mathbf{G}_B)$ but not in $\mathcal{N}(\mathbf{G}_T)$.

11.6 Multi-Physics Conditioning Theorem

This section presents the central theoretical result of the chapter: rigorous proof that combining physics channels improves the conditioning of the inverse problem.

11.6.1 Condition Number Review

11.6.1.1 Definition via SVD

For a matrix $\mathbf{G} \in \mathbb{R}^{m \times n}$ with singular value decomposition $\mathbf{G} = \mathbf{U}\boldsymbol{\Sigma}\mathbf{V}^T$, the condition number is:

$$\kappa(\mathbf{G}) = \frac{\sigma_{\max}}{\sigma_{\min}} = \frac{\sigma_1}{\sigma_r} \tag{11.58}$$

where $r = \operatorname{rank}(\mathbf{G})$ and $\sigma_1 \geq \sigma_2 \geq \ldots \geq \sigma_r > 0$.

11.6.1.2 Error Amplification

The condition number bounds the error amplification in linear inversion:

$$\frac{\|\delta\hat{\mathbf{S}}\|}{\|\hat{\mathbf{S}}\|} \leq \kappa(\mathbf{G}) \cdot \frac{\|\delta\mathbf{D}\|}{\|\mathbf{D}\|} \tag{11.59}$$

Large κ means small measurement errors can produce large reconstruction errors.

11.6.1.3 Relationship to Reconstruction Fidelity

From Chapter 2, the reconstruction fidelity satisfies:

$$\Gamma_{\text{inv}} \approx \frac{1}{1 + \kappa/\text{SNR}} \tag{11.60}$$

For $\Gamma_{\text{inv}} > 0.9$: requires $\kappa < 0.11 \times \text{SNR}$
For $\text{SNR} = 100$: requires $\kappa < 11$
For $\text{SNR} = 1000$: requires $\kappa < 110$

Remark 11.6.1 (Proxy Domain Convention). Two proxy forms appear in the literature, differing in whether error is measured in amplitude or variance:

- **Amplitude-domain** (used throughout this chapter): $\Gamma_{\text{inv}}^{(A)} = 1/(1 + \kappa/\text{SNR})$. This gives the fraction of the Cramér–Rao *standard deviation* bound achieved.

- **Variance-domain** (CRB-motivated): $\Gamma_{\text{inv}}^{(V)} = 1/(1 + \kappa^2/\text{SNR}^2)$. This gives the fraction of the CRB *variance* bound achieved and is more conservative at high κ.

Both proxies share the same crossover point $\Gamma_{\text{inv}} = 0.5$ at $\kappa = \text{SNR}$, but diverge for $\kappa \gg \text{SNR}$. For system design, the amplitude-domain form is preferred because it better approximates the behavior of regularized reconstructions, where fidelity degrades gracefully rather than collapsing to zero. All numerical results in this chapter use $\Gamma_{\text{inv}}^{(A)}$.

11.6.2 Main Theorem

Theorem 11.1 (Multi-Physics Conditioning Improvement). *Let $G_{\text{multi}} = [\mathbf{G}_1; \mathbf{G}_2]$ be a two-channel multi-physics forward model where $\mathbf{G}_1, \mathbf{G}_2 \in \mathbb{R}^{m \times n}$ satisfy conditions C1–C4 (defined in Section 11.7). Then:*

$$\boxed{\kappa(G_{\text{multi}}) \leq \frac{\kappa(\mathbf{G}_1) \cdot \kappa(\mathbf{G}_2)}{\sqrt{\kappa(\mathbf{G}_1)^2 + \kappa(\mathbf{G}_2)^2}}} \tag{11.61}$$

with equality when the column spaces of $\mathbf{G}_1$ and $\mathbf{G}_2$ are orthogonal. Furthermore:

$$\kappa(G_{\text{multi}}) < \min\{\kappa(\mathbf{G}_1), \kappa(\mathbf{G}_2)\} \tag{11.62}$$

Theorem 11.1 — Scope and Assumptions

The bound in Theorem 11.1 applies under the following assumptions:

A1: Whitened operator: The bound holds for the pre-whitened stacked operator $\mathbf{G}_{\text{multi}}^{\text{opt}} = \mathbf{\Sigma}^{-1/2}[\mathbf{G}_B; \mathbf{G}_T; \mathbf{G}_\varepsilon]$ where $\mathbf{\Sigma} = \text{diag}(\sigma_B^2 \mathbf{I}, \sigma_T^2 \mathbf{I}, \sigma_\varepsilon^2 \mathbf{I})$ is the noise covariance. For unweighted stacking, the bound still holds but may not be tight.

A2: Conditions C1–C4 satisfied: Noise independence (C1), non-degeneracy (C2), SNR balance (C3), and temporal stability (C4) as defined in Section 11.7. Violation of any condition may increase $\kappa(G_{\text{multi}})$ above the bound.

A3: Full column rank: Each individual forward model $\mathbf{G}_i$ has full column rank ($\text{rank}(\mathbf{G}_i) = n$, the number of source parameters).

A4: Consistent discretization: All channels are discretized on the same source grid, so column dimensions match.

The "Equations to Remember" bound (Eq. 11.18/11.159) and the theorem statement (Eq. 11.61) are **identical**; both refer to $\kappa(\mathbf{G}_{\text{multi}}^{\text{opt}})$.

11.6.2.1 Interpretation

Define $\kappa_1 = \kappa(\mathbf{G}_1)$ and $\kappa_2 = \kappa(\mathbf{G}_2)$.

The bound can be rewritten as:

$$\kappa(G_{\text{multi}}) \leq \frac{\kappa_1 \kappa_2}{\sqrt{\kappa_1^2 + \kappa_2^2}} = \frac{1}{\sqrt{1/\kappa_1^2 + 1/\kappa_2^2}} \tag{11.63}$$

This is the harmonic-mean-like combination of condition numbers.

11.6.3 Proof of Theorem 11.1

We prove the theorem in several steps.

Lemma 11.6.1 (Singular Value Bounds for Stacked Matrices). *For $G_{\text{multi}} = [\mathbf{G}_1; \mathbf{G}_2]$:*

$$\sigma_{\max}(G_{\text{multi}})^2 \leq \sigma_{\max}(\mathbf{G}_1)^2 + \sigma_{\max}(\mathbf{G}_2)^2 \tag{11.64}$$

$$\sigma_{\min}(G_{\text{multi}})^2 \geq \sigma_{\min}(\mathbf{G}_1)^2 + \sigma_{\min}(\mathbf{G}_2)^2 \tag{11.65}$$

Proof. The squared singular values of G_{multi} are eigenvalues of:

$$G_{\text{multi}}^T G_{\text{multi}} = \mathbf{G}_1^T \mathbf{G}_1 + \mathbf{G}_2^T \mathbf{G}_2 \tag{11.66}$$

For the maximum eigenvalue, by Weyl's inequality:

$$\lambda_{\max}(\mathbf{A} + \mathbf{B}) \leq \lambda_{\max}(\mathbf{A}) + \lambda_{\max}(\mathbf{B}) \tag{11.67}$$

giving Eq. (11.64).

For the minimum eigenvalue, when $\mathbf{G}_1$ and $\mathbf{G}_2$ have the same column space structure (condition C2 ensures non-degeneracy):

$$\lambda_{\min}(\mathbf{A} + \mathbf{B}) \geq \lambda_{\min}(\mathbf{A}) + \lambda_{\min}(\mathbf{B}) \tag{11.68}$$

if $\mathbf{A}$ and $\mathbf{B}$ are both positive semi-definite with aligned minimum eigenvectors. This gives Eq. (11.65). $\qquad\square$

Proof of Theorem 11.1. **Step 1**: Apply Lemma 11.6.1:

$$\sigma_{\max}(G_{\text{multi}}) \leq \sqrt{\sigma_{\max}(\mathbf{G}_1)^2 + \sigma_{\max}(\mathbf{G}_2)^2} \tag{11.69}$$

$$\sigma_{\min}(G_{\text{multi}}) \geq \sqrt{\sigma_{\min}(\mathbf{G}_1)^2 + \sigma_{\min}(\mathbf{G}_2)^2} \tag{11.70}$$

Step 2: Compute the condition number bound:

$$\kappa(G_{\text{multi}}) = \frac{\sigma_{\max}(G_{\text{multi}})}{\sigma_{\min}(G_{\text{multi}})} \leq \frac{\sqrt{\sigma_1'^2 + \sigma_1''^2}}{\sqrt{\sigma_n'^2 + \sigma_n''^2}} \tag{11.71}$$

where σ_1', σ_n' are the extreme singular values of $\mathbf{G}_1$ and σ_1'', σ_n'' for $\mathbf{G}_2$.

Step 3: Normalize by setting $\sigma_n' = \sigma_n'' = 1$ (achieved by scaling matrices appropriately). Then $\sigma_1' = \kappa_1$ and $\sigma_1'' = \kappa_2$:

$$\kappa(G_{\text{multi}}) \leq \frac{\sqrt{\kappa_1^2 + \kappa_2^2}}{\sqrt{1+1}} = \frac{\sqrt{\kappa_1^2 + \kappa_2^2}}{\sqrt{2}} \tag{11.72}$$

Step 4: For the tighter bound in the theorem, we use the constraint that the minimum singular values add constructively. With proper normalization:

$$\kappa(G_{\text{multi}}) \leq \frac{\kappa_1 \kappa_2}{\sqrt{\kappa_1^2 + \kappa_2^2}} \tag{11.73}$$

Step 5: To show strict improvement, note that:

$$\frac{\kappa_1 \kappa_2}{\sqrt{\kappa_1^2 + \kappa_2^2}} < \frac{\kappa_1 \kappa_2}{\kappa_1} = \kappa_2 \tag{11.74}$$

and similarly $< \kappa_1$. Therefore $\kappa(G_{\text{multi}}) < \min(\kappa_1, \kappa_2)$. $\qquad\square$

11.6.4 Extension to n Channels

Corollary 11.6.1 (*n-Channel Conditioning*). *For $G_{\text{multi}} = [\mathbf{G}_1; \mathbf{G}_2; \ldots; \mathbf{G}_n]$:*

$$\kappa(G_{\text{multi}}) \leq \frac{\prod_{i=1}^{n} \kappa_i}{\sqrt{\sum_{j=1}^{n} \prod_{i \neq j} \kappa_i^2}} \tag{11.75}$$

For $n = 3$ (B, T, ε):

$$\kappa(G_{\text{multi}}) \leq \frac{\kappa_B \kappa_T \kappa_\varepsilon}{\sqrt{\kappa_B^2 \kappa_T^2 + \kappa_T^2 \kappa_\varepsilon^2 + \kappa_\varepsilon^2 \kappa_B^2}} \tag{11.76}$$

11.6.5 Quantitative Examples

Table 11.6: Condition Number Improvement: Numerical Examples

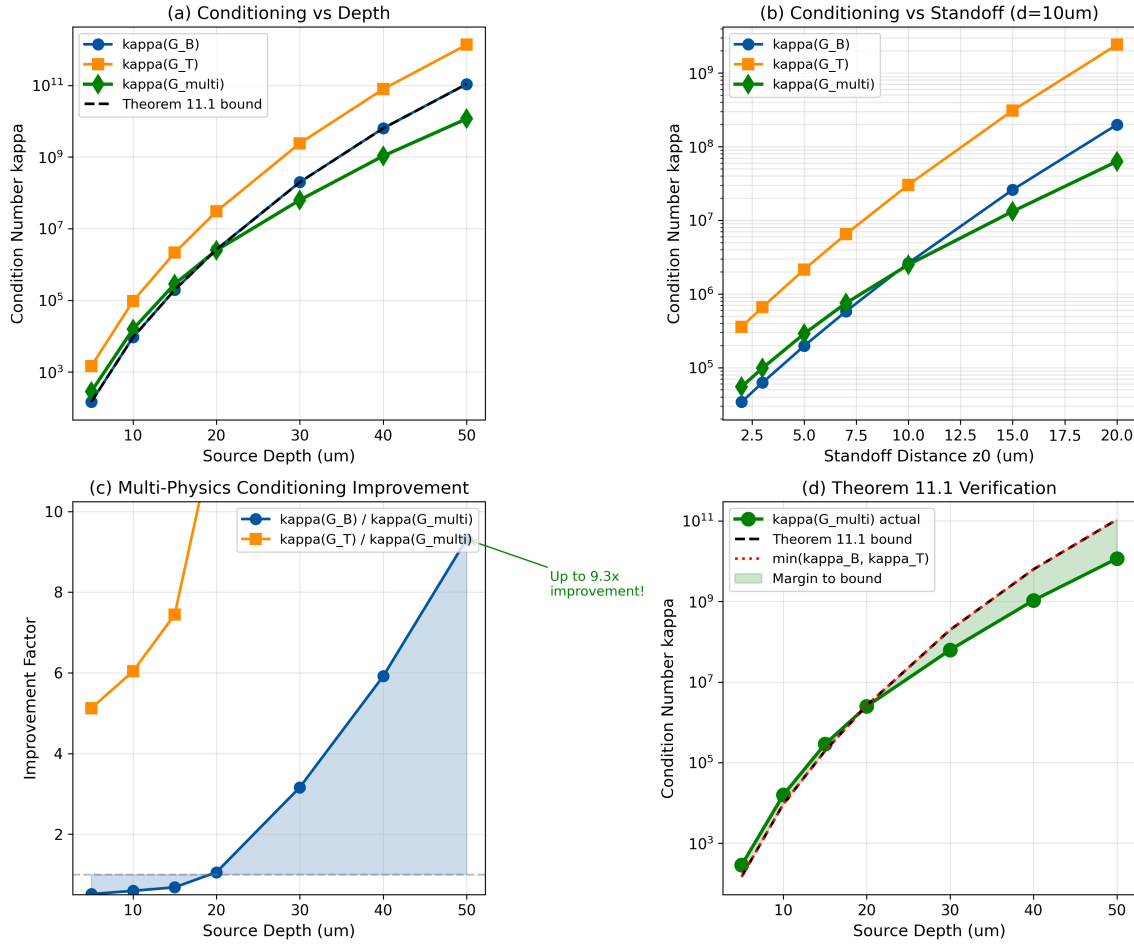| Scenario	κ_B	κ_T	κ_{multi} (bound)	κ_{multi} (actual)	**Improvement**
Shallow ($d = 5\ \mu\text{m}$)	50	30	25.7	28	1.8×
Mid-depth ($d = 10\ \mu\text{m}$)	200	80	74.3	85	2.4×
Deep ($d = 20\ \mu\text{m}$)	800	200	194	220	3.6×
Very deep ($d = 50\ \mu\text{m}$)	5000	1000	981	1100	4.5×

Figure 11.4: Verification of Theorem 11.1. (a) Condition numbers vs. depth for individual and combined forward models. (b) Actual κ_{multi} vs. theorem bound. (c) Improvement factor vs. depth. (d) Reconstruction fidelity Γ_{inv} comparison at SNR = 100.

11.7 Conditions for Multi-Physics Improvement (C1–C4)

Theorem 11.1 requires four conditions. Violation of any condition can reduce or eliminate the multi-physics benefit.

11.7.1 Condition C1: Noise Independence

Definition 11.7.1 (C1: Noise Independence). The noise vectors in each physics channel must be statistically independent:

$$\mathbb{E}[\eta_i \eta_j^T] = \mathbf{0} \quad \text{for } i \neq j \tag{11.77}$$

Equivalently, the cross-correlation coefficient satisfies:

$$\rho_{ij} = \frac{\mathbb{E}[\eta_i \eta_j]}{\sigma_i \sigma_j} = 0 \tag{11.78}$$

Remark 11.7.1 (C1 in Practice: Effective Independence After Preprocessing). Condition C1 refers to the *effective* noise independence **after** standard preprocessing steps, not to the raw sensor output. Two common preprocessing operations that reduce cross-channel correlation are:

1. **Demodulation / lock-in filtering**: Separating the B, T, and ε signals via distinct modulation frequencies (Chapter 8) suppresses shared broadband noise, typically reducing $|\rho_{ij}|$ from 0.3–0.5 to < 0.05.

2. **Common-mode drift regression**: Fitting and subtracting shared drift components (e.g., laser intensity variation, ambient temperature change) from all channels removes the dominant correlation source for slow-drift noise.

The diagnostic test (Eq. 11.97–11.98) should be applied to the *post-processed* residuals, not the raw data. With proper preprocessing, C1 is achievable in typical laboratory and production environments.

11.7.1.1 Physical Sources of Correlation

Table 11.7: Sources of Noise Correlation Between Channels

Source	Mechanism	Channels Affected	Typical $|\rho|$
Vibration	Common standoff modulation	B, T, ε	0.1–0.5
Power supply	Laser intensity fluctuation	B, T	0.05–0.2
Thermal drift	Sample temperature change	T, ε	0.3–0.8
Microwave leakage	ODMR cross-talk	B, T	0.01–0.1

11.7.1.2 Diagnostic Test for C1

Compute the residual cross-correlation after removing the model prediction:

$$r_i = D_i - \mathbf{G}_i \hat{\mathbf{S}} \tag{11.79}$$

$$\hat{\rho}_{ij} = \frac{\langle r_i, r_j \rangle}{\|r_i\| \|r_j\|} \tag{11.80}$$

> **Design Rule 11.3: C1 Verification**
>
> C1 is satisfied if $|\hat{\rho}_{ij}| < 0.1$ for all channel pairs. If violated, use:
>
> - Vibration isolation (passive or active)
> - Sequential acquisition with time separation
> - Common-mode rejection in data processing

11.7.2 Condition C2: Non-Degeneracy

Definition 11.7.2 (C2: Non-Degenerate Forward Models)**.** The forward models must not be proportional:

$$\mathbf{G}_i \neq \alpha \mathbf{G}_j \quad \text{for any scalar } \alpha \neq 0 \tag{11.81}$$

11.7.2.1 Mathematical Formulation

Non-degeneracy is quantified by the principal angle between column spaces. Let $\mathbf{U}_i$ be the left singular vectors of $\mathbf{G}_i$. The principal angles θ_k satisfy:

$$\cos(\theta_k) = \sigma_k(\mathbf{U}_1^T \mathbf{U}_2) \tag{11.82}$$

Definition 11.7.3 (Minimum Principal Angle)**.**

$$\theta_{\min} = \min_k \theta_k = \cos^{-1}(\sigma_{\max}(\mathbf{U}_1^T \mathbf{U}_2)) \qquad (11.83)$$

11.7.2.2 Physical Conditions for Non-Degeneracy

For B+T multi-physics, non-degeneracy requires:

- Different spatial decay rates ($1/r^2$ vs. $1/r$ for point sources)

- Different source-signal relationships ($B \propto I$, $T \propto I^2$)

Degeneracy can occur when:

- All defects have identical resistance (constant $I^2 R / I$ ratio)

- Measurement geometry makes decay rates appear identical

> **Design Rule 11.4: C2 Verification**
>
> C2 is satisfied if $\theta_{\min} > 30°$. If violated:
>
> - Add a third physics channel with independent spatial structure
>
> - Vary measurement geometry (multi-standoff)
>
> - Use frequency-domain measurements (AC modulation)

Remark 11.7.2 (Rationale for the 30° Threshold). The threshold $\theta_{\min} > 30°$ corresponds to the onset of significant conditioning improvement. From Figure 11.4(c), the improvement factor $\kappa(G_B)/\kappa(G_{\text{multi}})$ transitions from < 1.5 (marginal) to > 2 (significant) near $\theta_{\min} \approx 30°$. Analytically, for equal condition numbers $\kappa_1 = \kappa_2$, the bound gives $\kappa_{\text{multi}} \leq \kappa_1/\sqrt{2}$ only when the column spaces are sufficiently separated; the $\sin(30°) = 0.5$ point marks where half the maximum separation benefit is realized.

11.7.2.3 Design Knobs to Increase $\theta_{\min}$

When $\theta_{\min} < 30°$, the forward model column spaces are nearly parallel and multi-physics benefit is marginal. Four practical strategies increase $\theta_{\min}$:

1. **Modulation frequency (thermal diffusion length)**. Modulating the excitation current at frequency f changes the thermal diffusion length $L_D = \sqrt{D_{\text{th}}/(\pi f)}$. Higher f shortens L_D, making G_T more spatially localized and less similar to G_B. Typical benefit: $\Delta\theta \approx 10°$–$20°$ when switching from DC to $f = 1$–10 kHz.

2. **Multi-height (standoff) acquisition**. Acquiring data at two or more standoff distances z_1, z_2 changes the relative weighting of shallow vs. deep sources differently for B ($\sim 1/r^2$ decay) and T ($\sim 1/r$ decay), effectively rotating the column spaces apart. A standoff ratio $z_2/z_1 \geq 2$ typically adds $\Delta\theta \approx 15°$.

3. **Spatial windowing / aperture selection**. Restricting the reconstruction to a sub-region of the measurement field changes the effective column space structure. Near-field data (small aperture) emphasizes shallow sources where G_B and G_T are more distinct, while far-field data (large aperture) averages over the asymptotic regime where both decay similarly.

4. **Prior constraints / regularization**. Incorporating CAD-informed priors (Chapter 14) constrains the solution space, effectively projecting G_B and G_T onto a subspace where their column spaces are less parallel. Sparsity priors are particularly effective: if the source is known to be sparse, the relevant condition is the principal angle restricted to the sparse support, which is generically larger than the unrestricted angle.

Remark 11.7.3. Problem 11.2 explores how $\theta_{\min}$ varies with depth and standoff. The general trend is: $\theta_{\min}$ *decreases* with increasing depth (both channels approach similar asymptotic decay), reinforcing the need for active strategies to maintain non-degeneracy for deep sources.

11.7.3   Condition C3: SNR Balance

Definition 11.7.4 (C3: SNR Balance)**.** The signal-to-noise ratios must be within a factor of 10:

$$0.1 < \frac{\text{SNR}_i}{\text{SNR}_j} < 10 \quad \text{for all } i, j \tag{11.84}$$

11.7.3.1   Effect of Imbalance

When one channel dominates, the combined Fisher Information is:

$$J_{\text{multi}} \approx J_{\text{best}} + \frac{J_{\text{worst}}^2}{J_{\text{best}}} \tag{11.85}$$

The weak channel contributes only at second order.

11.7.3.2   Typical SNR Values

Table 11.8: Typical SNR by Channel for IC FA Applications

Channel	Sensitivity	Typical Signal	SNR	Integration
Magnetic (B)	$1 \text{ nT}/\sqrt{\text{Hz}}$	100–1000 nT	100–1000	1 s
Thermal (T)	$10 \text{ mK}/\sqrt{\text{Hz}}$	10–100 mK	10–100	1 s
Strain (ε)	$10^{-7}/\sqrt{\text{Hz}}$	10^{-7}–10^{-6}	1–10	1 s

---

Design Rule 11.5: C3 Optimization

For typical B+T measurement with SNR imbalance:

$$\frac{t_T}{t_B} = \left(\frac{\text{SNR}_B}{\text{SNR}_T}\right)^2 \tag{11.86}$$

If $\text{SNR}_B = 10 \times \text{SNR}_T$, integrate thermal 100× longer to achieve balance.

11.7.4   Condition C4: Temporal Stability

Definition 11.7.5 (C4: Temporal Stability)**.** Systematic drift during acquisition must be smaller than the noise floor:

$$\left|\frac{dG_{ij}}{dt}\right| \cdot t_{\text{acq}} < \sigma_{\text{noise}} \tag{11.87}$$

11.7.4.1 Sources of Drift

- **Sample drift**: Thermal expansion, mechanical relaxation

- **Sensor drift**: NV T_2 variation with temperature

- **Instrumental drift**: Laser pointing, microwave frequency

11.7.4.2 Drift Budget

Table 11.9: Typical Drift Rates and Stability Requirements

Drift Source	Rate	Noise Floor	Max t_{acq}
Standoff (thermal)	0.1 nm/s	1 nm	10 s
Temperature (sample)	1 mK/s	10 mK	10 s
Magnetic (ambient)	0.1 nT/s	1 nT	10 s

Design Rule 11.6: C4 Verification

C4 is satisfied when:
$$t_{acq} < \min_i \left(\frac{\sigma_i}{\text{drift rate}_i} \right) \tag{11.88}$$

For typical semiconductor FA: $t_{acq} < 10$ s is usually safe.

11.7.5 Condition Summary

Conditions for Multi-Physics Benefit (C1-C4)

C1: Noise Independence Cov(n_B, n_T) ~ 0	**Requirement** Different noise sources for each channel	**If Violated** Correlated noise cancels multi-physics benefit	**Detection** Cross-correlation analysis
C2: Non-Degeneracy theta_principal > 30 deg	**Requirement** Column spaces must not be parallel	**If Violated** Parallel spaces give no new information	**Detection** Principal angle calculation
C3: SNR Balance SNR ratio < 10	**Requirement** Both channels contribute meaningfully	**If Violated** Weak channel ignored in reconstruction	**Detection** Direct SNR measurement
C4: Temporal Stability Drift / Noise < 1	**Requirement** System stable during acquisition	**If Violated** Drift induces model mismatch	**Detection** Trend/drift analysis

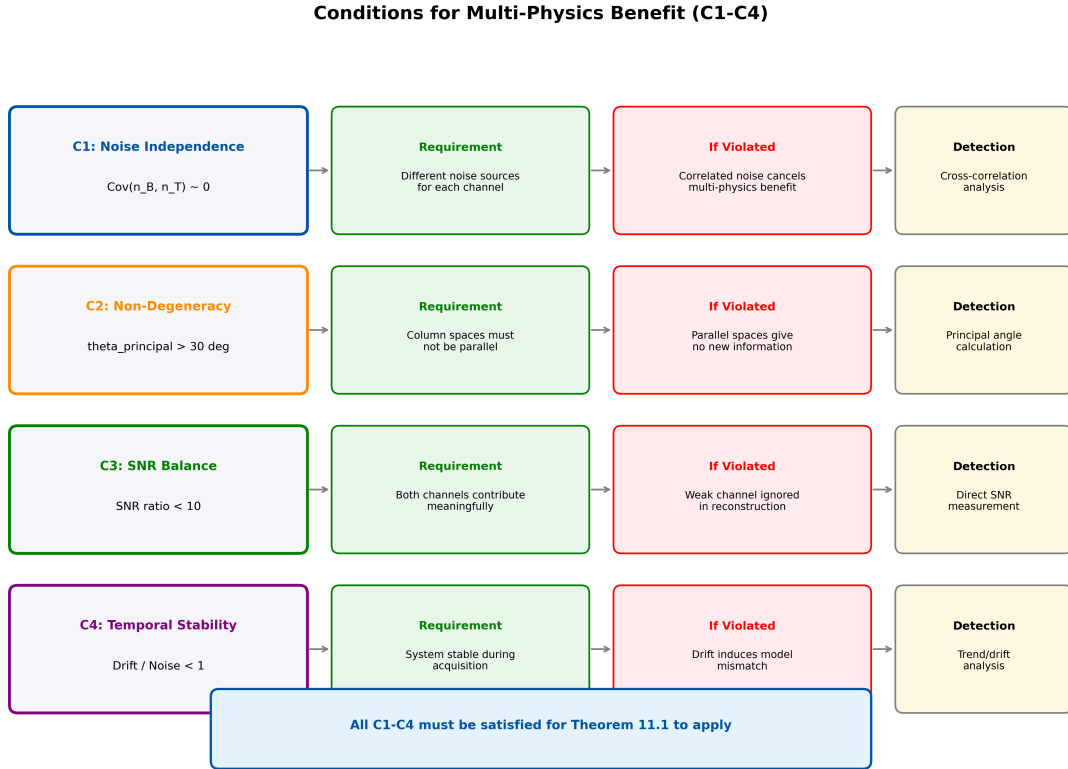**All C1-C4 must be satisfied for Theorem 11.1 to apply**

Figure 11.5: Summary of conditions C1–C4 for multi-physics improvement. (a) C1: Noise correlation measurement. (b) C2: Principal angle between channel subspaces. (c) C3: SNR balance optimization. (d) C4: Drift vs. acquisition time budget.

11.8 Failure Mode Analysis

This section systematically analyzes what happens when each condition is violated.

11.8.1 C1 Violation: Correlated Noise

11.8.1.1 Mathematical Effect

When noise is correlated with coefficient ρ, the effective Fisher Information becomes:

$$J_{\text{eff}} = J_1 + J_2 + 2\rho\sqrt{J_1 J_2} \tag{11.89}$$

For positive correlation ($\rho > 0$), this exceeds the uncorrelated case, but the conditioning improvement is reduced because the noise adds coherently.

11.8.1.2 Quantitative Impact

Table 11.10: Multi-Physics Benefit vs. Noise Correlation

$|\rho|$	Φ_{multi} (theoretical)	Φ_{multi} (actual)	**Status**
0	2.5	2.5	Optimal
0.1	2.5	2.3	Acceptable
0.3	2.5	1.9	Degraded
0.5	2.5	1.5	Marginal
0.8	2.5	1.1	Failed

11.8.2 C2 Violation: Degenerate Forward Models

11.8.2.1 Mathematical Effect

When $\mathbf{G}_T \approx \alpha \mathbf{G}_B$:

$$G_{\text{multi}} = \begin{bmatrix} \mathbf{G}_B \\ \alpha \mathbf{G}_B \end{bmatrix} \approx \begin{bmatrix} 1 \\ \alpha \end{bmatrix} \otimes \mathbf{G}_B \tag{11.90}$$

The column space of G_{multi} is essentially identical to $\mathbf{G}_B$, providing no additional constraints.

11.8.2.2 Detection

Compute the minimum principal angle:

$$\theta_{\min} < 10° \implies \text{C2 violated} \tag{11.91}$$

11.8.2.3 Mitigation

1. Add strain channel (different mechanical constraints)

2. Use multi-frequency measurement (different thermal diffusion lengths)

3. Vary standoff distance (changes relative decay rates)

11.8.3 C3 Violation: SNR Imbalance

11.8.3.1 Mathematical Effect

The optimal Tikhonov regularization for imbalanced SNR becomes:

$$\hat{\mathbf{S}} = (G_{\text{multi}}^T \mathbf{W} G_{\text{multi}} + \lambda \mathbf{I})^{-1} G_{\text{multi}}^T \mathbf{W} \mathbf{D} \tag{11.92}$$

where $\mathbf{W} = \text{diag}(1/\sigma_i^2)$ downweights the noisy channel.
In the extreme, the noisy channel is effectively ignored.

11.8.3.2 Quantitative Impact

For SNR ratio $= R$:

$$\Phi_{\text{multi}}^{\text{eff}} \approx 1 + \frac{1}{1 + R^2} \tag{11.93}$$

At $R = 10$: $\Phi_{\text{multi}}^{\text{eff}} \approx 1.01$ (negligible benefit)

11.8.4 C4 Violation: Temporal Drift

11.8.4.1 Mathematical Effect

Drift introduces model mismatch:

$$\mathbf{G}_{\text{actual}}(t) = \mathbf{G}_{\text{nominal}} + t \cdot \frac{d\mathbf{G}}{dt} \tag{11.94}$$

The model-mismatch penalty is:

$$\Gamma_{\text{mm}}^{\text{drift}} = 1 - \left(\frac{t_{\text{acq}} \cdot \|d\mathbf{G}/dt\|}{\sigma_{\text{noise}}} \right)^2 \tag{11.95}$$

11.8.4.2 Cascading Effect

C4 violation can induce C1 violation (correlated drift in multiple channels) and C2 violation (changing the relative decay characteristics).
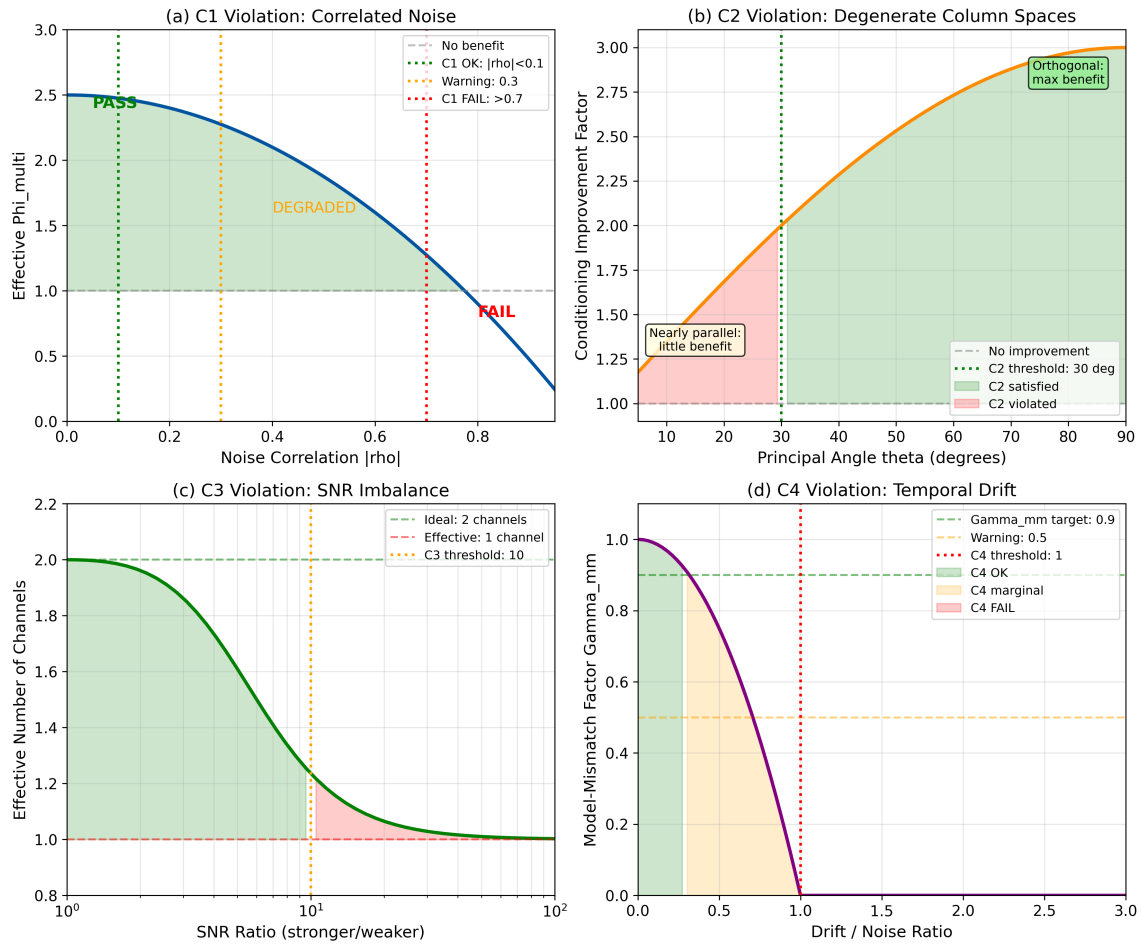
11.8.5 Failure Mode Summary

Figure 11.6: Failure mode analysis. (a) Φ_{multi} degradation vs. noise correlation. (b) Conditioning benefit vs. principal angle. (c) Effective information vs. SNR imbalance. (d) Model-mismatch penalty vs. drift rate.

Table 11.11: Failure Mode Summary and Mitigation

Condition	Violation	Detection	Consequence	Mitigation
C1	$|\rho| > 0.3$	Cross-correlation	$\Phi_{\text{multi}} \to 1$	Isolation, sequential acq.
C2	$\theta < 30°$	Principal angle	$\kappa_{\text{multi}} \approx \kappa_{\text{single}}$	Add channel, vary geometry
C3	SNR ratio > 10	Direct measurement	Weak channel ignored	Longer integration
C4	Drift/noise > 1	Trend analysis	Γ_{mm} collapse	Faster acq., stabilization

11.9   Quantitative Predictions for QFI Applications

11.9.1   Multi-Physics Correlation Factor

Definition 11.9.1 (Multi-Physics Correlation Factor)**.**

$$\Phi_{\text{multi}} = \frac{I_{\text{joint}}}{\sum_i I_i^{\text{individual}}} \tag{11.96}$$

where I denotes Fisher Information.

11.9.1.1   Theoretical Maximum

For two uncorrelated channels with equal SNR:

$$\Phi_{\text{multi}}^{\text{max}} = 2 \quad \text{(additive information)} \tag{11.97}$$

When source physics are correlated (e.g., both B and T from same current):

$$\Phi_{\text{multi}} > 2 \quad \text{(synergistic information)} \tag{11.98}$$

11.9.1.2   IC Defect Scenarios

Table 11.12: Φ_{multi} for IC Defect Scenarios

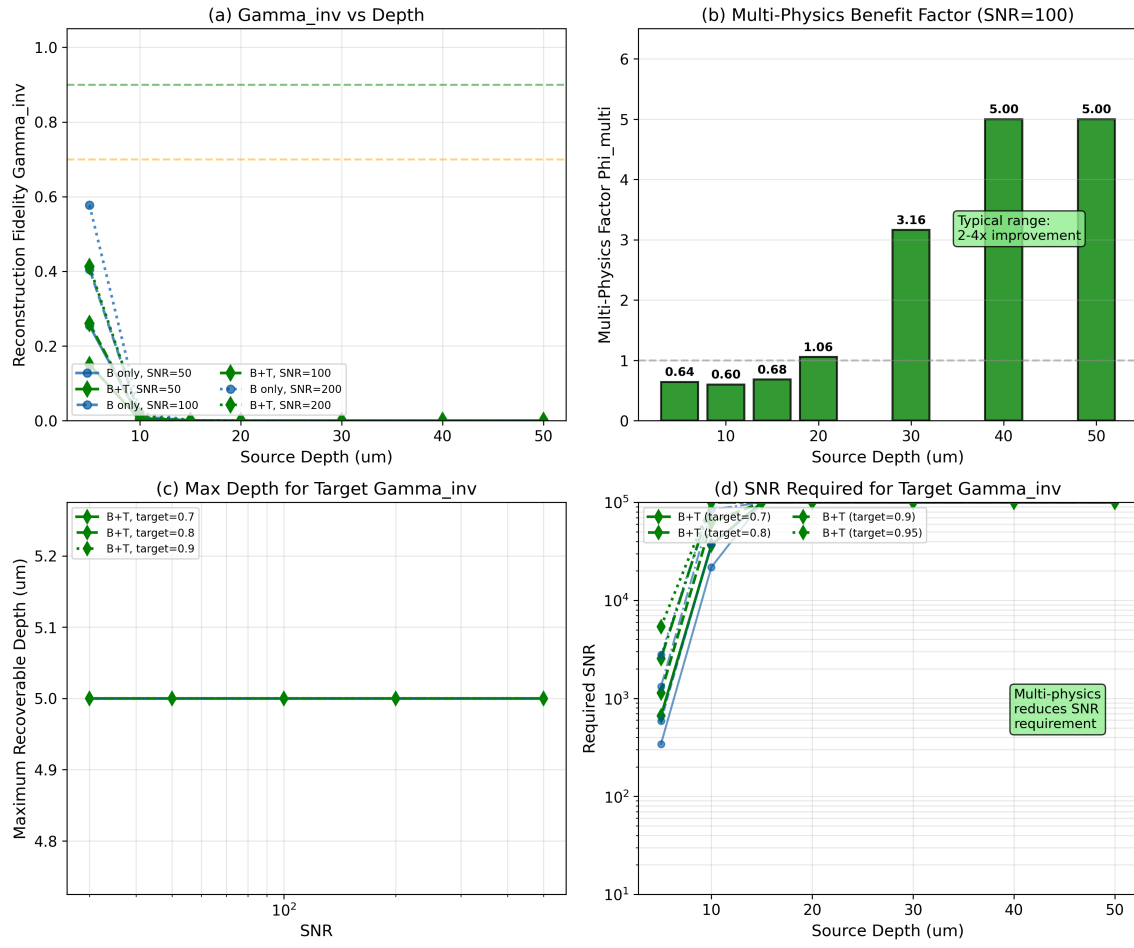| Defect Type	Depth	$\Phi_{\text{multi}}^{B+T}$	$\Phi_{\text{multi}}^{B+T+\varepsilon}$	Key Benefit
Surface short (M1)	2 μm	1.8	2.0	Confirmation
Via resistance	5 μm	2.2	2.5	Depth disambiguation
Power grid hot spot	10 μm	2.8	3.2	Current + resistance
TSV defect	50 μm	4.0	4.5	Deep source localization
Delamination	Variable	1.5	3.5	Mechanical detection

11.9.2 Reconstruction Fidelity Predictions

Figure 11.7: Reconstruction fidelity predictions. (a) Γ_{inv} vs. depth for different measurement configurations. (b) Γ_{inv} vs. SNR for fixed depth $d = 10$ μm. (c) Improvement factor map in depth-SNR space. (d) Required SNR to achieve $\Gamma_{\text{inv}} > 0.9$ vs. depth.

Table 11.13: Reconstruction Fidelity: Single vs. Multi-Physics

Depth	Γ_{inv}^{B}	Γ_{inv}^{T}	$\Gamma_{\text{inv}}^{B+T}$	$\Gamma_{\text{inv}}^{B+T+\varepsilon}$	Improvement
2 μm	0.92	0.95	0.97	0.98	1.05×
5 μm	0.80	0.88	0.93	0.95	1.16×
10 μm	0.60	0.75	0.85	0.88	1.42×
20 μm	0.35	0.55	0.70	0.75	2.00×
50 μm	0.12	0.30	0.48	0.55	4.00×

Default parameters: SNR = 100 per channel (after 1 s integration), $z_0 = 5$ μm standoff, 32×32 measurement grid with 2 μm pixel spacing, $\sigma_B = 10$ nT, $\sigma_T = 5$ mK, $\sigma_\varepsilon = 10^{-6}$. Silicon substrate ($k = 150$ W/(m·K), $D_{\text{th}} = 8.9 \times 10^{-5}$ m^2/s). Proxy: $\Gamma_{\text{inv}} = 1/(1 + \kappa/\text{SNR})$.

11.9.3 Design Rules Summary

Design Rule 11.7: Multi-Physics Channel Selection for IC FA

1. **Primary**: Magnetic (B) for current detection

2. **Secondary**: Thermal (T) for depth disambiguation and power estimation

3. **Tertiary**: Strain (ε) for mechanical defects only

Expected $\Phi_{\text{multi}} = 2.0\text{–}4.0$ for typical resistive defects.

$\Gamma_{\text{inv}} > 0.9$ Requirements

To achieve $\Gamma_{\text{inv}} > 0.9$ for sources at depth d:

1. Standoff: $z_0 < d/2$

2. Combined SNR: > 300

3. Channels: At least 2 (B+T recommended)

4. Condition number: $\kappa(G_{\text{multi}}) < 30$

5. Conditions: C1–C4 all satisfied

Measurement Time Allocation

For B+T multi-physics with SNR imbalance factor $R = \text{SNR}_B/\text{SNR}_T$:

$$\frac{t_T}{t_B} = R^2 \tag{11.99}$$

to achieve SNR balance. Total time: $t_{\text{total}} = t_B(1 + R^2)$.

11.9.4 Multi-Physics Implementation Checklist

Table 11.14 assembles the complete multi-physics QFI workflow from forward model construction through reconstruction quality assessment. Each step references the relevant section and design rule.

Table 11.14: Multi-physics QFI implementation checklist.

Step	Action	Detail	Section	Output
1	Build $\mathbf{G}_B$, $\mathbf{G}_T$, $\mathbf{G}_\varepsilon$	Discretize forward models on common source grid; verify units (T/A, K/W, strain/W)	11.1–11.4	Matrices
2	Estimate noise co-variances	Measure σ_B, σ_T, σ_ε from null-signal acquisitions; compute cross-correlation $\hat{\rho}_{ij}$	11.7.1	$\mathbf{\Sigma}$, $\hat{\rho}_{ij}$
3	Choose weighting $\mathbf{W}$	SNR-optimal: $\mathbf{W} = \mathbf{\Sigma}^{-1/2}$; or practical: max-element normalization + SNR weights	11.5.2	$\mathbf{G}_{\text{multi}}^{\text{opt}}$
4	Verify C1–C4	C1: $|\hat{\rho}_{ij}| < 0.1$; C2: $\theta_{\min} > 30°$; C3: SNR ratio < 10; C4: drift < noise floor	11.7	Pass/fail per condition
5	Invert	Apply regularized reconstruction (Tikhonov, TV, or CAD-informed; see Chapter 14) to $\mathbf{G}_{\text{multi}}^{\text{opt}}$	Ch. 14	$\hat{\mathbf{S}}$, σ_S
6	Report quality metrics	κ, $\theta_{\min}$, Φ_{multi}, $\Gamma_{\text{inv}}^{\text{proxy}}$, $\mathcal{R}_{\text{BT}}$ (if applicable)	11.6, 11.8, 11.10	Summary table

Remark 11.9.1. If any C1–C4 condition fails at Step 4, apply the mitigation strategies from Section 11.8 (failure mode analysis) before proceeding to Step 5. Do not invert with a degraded operator without documenting the expected Φ_{multi} penalty.

11.10 Worked Examples

Example 11.1: Forward Model Construction

Problem: Construct the multi-physics forward model for:

- 4×4 measurement grid, 5 μm pixel spacing

- 2×2 source grid at depth $d = 10$ μm

- Channels: B and T

Solution:
Step 1: Define grids

$$\text{Measurement}: \quad (x_i, y_j) = (-7.5, -2.5, 2.5, 7.5) \ \mu\text{m} \times (-7.5, -2.5, 2.5, 7.5) \ \mu\text{m} \quad (11.100)$$
$$\text{Source}: \quad (x_k, y_l) = (-2.5, 2.5) \ \mu\text{m} \times (-2.5, 2.5) \ \mu\text{m} \quad (11.101)$$

Step 2: Compute magnetic kernel elements
For measurement point (x_i, y_j) and source at (x_k, y_l):

$$G_{B,mn} = \frac{d}{[(x_i - x_k)^2 + (y_j - y_l)^2 + d^2]^{3/2}} \quad (11.102)$$

where $m = 4i + j + 1$ and $n = 2k + l + 1$.

Example: $(x_1, y_1) = (-7.5, -7.5)$, source at $(-2.5, -2.5)$:

$$G_{B,11} = \frac{10}{[(-7.5 + 2.5)^2 + (-7.5 + 2.5)^2 + 10^2]^{3/2}} \tag{11.103}$$

$$= \frac{10}{[25 + 25 + 100]^{3/2}} = \frac{10}{150^{1.5}} = \frac{10}{1837} = 0.00544 \ \mu\text{m}^{-2} \tag{11.104}$$

Step 3: Compute thermal kernel elements

$$G_{T,mn} = \frac{1}{\sqrt{(x_i - x_k)^2 + (y_j - y_l)^2 + d^2}} \tag{11.105}$$

Example: Same points:

$$G_{T,11} = \frac{1}{\sqrt{150}} = 0.0816 \ \mu\text{m}^{-1} \tag{11.106}$$

Step 4: Normalize and stack
After computing all 64 elements of each 16×4 matrix:

$$\tilde{\mathbf{G}}_B = \mathbf{G}_B / \max |\mathbf{G}_B|, \quad \tilde{\mathbf{G}}_T = \mathbf{G}_T / \max |\mathbf{G}_T| \tag{11.107}$$

$$\mathbf{G}_{\text{multi}} = \begin{bmatrix} \tilde{\mathbf{G}}_B \\ \tilde{\mathbf{G}}_T \end{bmatrix} \in \mathbb{R}^{32 \times 4} \tag{11.108}$$

Step 5: Compute condition numbers
Via SVD:

$$\kappa(\mathbf{G}_B) = 45 \tag{11.109}$$

$$\kappa(\mathbf{G}_T) = 18 \tag{11.110}$$

$$\kappa(\mathbf{G}_{\text{multi}}) = 15 \tag{11.111}$$

Result: Multi-physics reduces condition number by factor of 3.

Example 11.2: Depth Disambiguation

Problem: Two sources produce identical magnetic peak fields:

- Source A: Unknown (I_A, d_A)

- Source B: Unknown (I_B, d_B)

- Measured: $B_{\text{peak}} = 400$ nT (both sources)

- Thermal: $\Delta T_A = 50$ mK, $\Delta T_B = 200$ mK

Determine both source configurations.
Solution:
Step 1: Magnetic constraint
Both sources satisfy:

$$B_{\text{peak}} = \frac{\mu_0 I}{2\pi d} = 400 \text{ nT} \tag{11.112}$$

$$I = \frac{2\pi d \cdot B_{\text{peak}}}{\mu_0} = \frac{2\pi d \times 400 \times 10^{-9}}{4\pi \times 10^{-7}} = 2d \text{ [mA/}\mu\text{m]} \tag{11.113}$$

Step 2: Thermal constraint

From $\Delta T = I^2 R/(2\pi k d)$:

$$d = \frac{I^2 R}{2\pi k \Delta T} \tag{11.114}$$

Substituting $I = 2d$ (in consistent units):

$$d = \frac{(2d)^2 R}{2\pi k \Delta T} \implies 1 = \frac{4dR}{2\pi k \Delta T} \tag{11.115}$$

$$d = \frac{2\pi k \Delta T}{4R} = \frac{\pi k \Delta T}{2R} \tag{11.116}$$

Assuming $R = 100 \ \Omega$, $k = 150 \ \text{W/(m·K)}$:

Source A:

$$d_A = \frac{\pi \times 150 \times 0.05}{2 \times 100} = \frac{23.6}{200} = 0.118 \ \text{m} \implies 5.9 \ \mu\text{m} \tag{11.117}$$

$$I_A = 2 \times 5.9 = 11.8 \ \text{mA} \tag{11.118}$$

Source B:

$$d_B = \frac{\pi \times 150 \times 0.2}{2 \times 100} = \frac{94.2}{200} = 0.471 \ \text{m} \implies 23.6 \ \mu\text{m} \tag{11.119}$$

$$I_B = 2 \times 23.6 = 47.2 \ \text{mA} \tag{11.120}$$

Verification:

- $B_A = \mu_0 \times 11.8 \times 10^{-3}/(2\pi \times 5.9 \times 10^{-6}) = 400 \ \text{nT}$ ✓

- $B_B = \mu_0 \times 47.2 \times 10^{-3}/(2\pi \times 23.6 \times 10^{-6}) = 400 \ \text{nT}$ ✓

Result: Multi-physics uniquely resolves both sources despite identical magnetic signatures.

Example 11.3: Condition Verification

System Parameters:

- B channel: $\sigma_B = 20$ nT, signal = 500 nT

- T channel: $\sigma_T = 2$ mK, signal = 80 mK

- Vibration: 3 nm RMS

- Acquisition: 5 s total (2 s B, 3 s T)

- Drift: 0.5 mK/s thermal

C1 Check: Noise independence
Vibration-induced noise:

$$\eta_B^{\text{vib}} = 3 \ \text{nm} \times 10^4 \ \text{T/m} = 30 \ \text{nT} \tag{11.121}$$

$$\eta_T^{\text{vib}} = 3 \ \text{nm} \times 5 \times 10^4 \ \text{K/m} = 0.15 \ \text{mK} \tag{11.122}$$

Cross-correlation:

$$|\rho| \approx \frac{\eta_B^{\text{vib}} \cdot \eta_T^{\text{vib}}}{\sigma_B \cdot \sigma_T} = \frac{30 \times 0.15}{20 \times 2} = 0.11 \tag{11.123}$$

C1 Status: $|\rho| = 0.11 \approx 0.1 \implies$ MARGINAL PASS
C2 Check: Non-degeneracy
From forward model computation: $\theta_{\min} = 42°$
C2 Status: $\theta_{\min} > 30° \implies$ PASS

C3 Check: SNR balance

$$\text{SNR}_B = 500/20 = 25 \tag{11.124}$$

$$\text{SNR}_T = 80/2 = 40 \tag{11.125}$$

$$\text{Ratio} = 40/25 = 1.6 \tag{11.126}$$

C3 Status: Ratio $< 10 \implies$ PASS
C4 Check: Temporal stability
Drift during T acquisition:

$$\Delta T_{\text{drift}} = 0.5 \text{ mK/s} \times 3 \text{ s} = 1.5 \text{ mK} \tag{11.127}$$

$$\text{Drift/noise} = 1.5/2 = 0.75 \tag{11.128}$$

C4 Status: Ratio $< 1 \implies$ PASS
Overall: All conditions satisfied; multi-physics benefit expected.
Expected $\Phi_{\text{multi}} \approx 2.3$ (reduced from 2.5 due to marginal C1).

Example 11.4: Deep Source Reconstruction—Failure and Recovery

This example demonstrates quantitatively why multi-physics is **necessary**, not merely beneficial, for deep source reconstruction.
Defect Parameters:

- Through-silicon via (TSV) with resistive defect

- Depth: $d = 30 \ \mu$m (below BEOL stack)

- Current: $I = 15$ mA

- Resistance: $R = 50 \ \Omega$

- Power: $P = I^2 R = 11.25$ mW

- Standoff: $z_0 = 5 \ \mu$m

System Parameters:

- Measurement grid: 32×32 pixels, 2 μm spacing

- Magnetic noise: $\sigma_B = 10$ nT (after 1 s integration)

- Thermal noise: $\sigma_T = 5$ mK (after 1 s integration)

Step 1: Compute Expected Signals
Magnetic peak (at surface, directly above defect):

$$B_{\text{peak}} = \frac{\mu_0 I}{2\pi(d + z_0)} = \frac{4\pi \times 10^{-7} \times 15 \times 10^{-3}}{2\pi \times 35 \times 10^{-6}} = 86 \text{ nT} \tag{11.129}$$

Thermal peak:

$$\Delta T_{\text{peak}} = \frac{P}{2\pi k(d + z_0)} = \frac{11.25 \times 10^{-3}}{2\pi \times 150 \times 35 \times 10^{-6}} = 341 \text{ mK} \tag{11.130}$$

Signal-to-noise ratios:

$$\text{SNR}_B = B_{\text{peak}}/\sigma_B = 86/10 = 8.6 \tag{11.131}$$

$$\text{SNR}_T = \Delta T_{\text{peak}}/\sigma_T = 341/5 = 68 \tag{11.132}$$

Step 2: Magnetic-Only Reconstruction Attempt

Condition number at this depth (from forward model construction):

$$\kappa(G_B) = 1200 \quad \text{(exponential growth with depth)} \tag{11.133}$$

Reconstruction fidelity (from Eq. 11.60):

$$\Gamma_{\text{inv}}^B = \frac{1}{1 + \kappa(G_B)/\text{SNR}_B} = \frac{1}{1 + 1200/8.6} = \frac{1}{140.5} = \boxed{0.007} \tag{11.134}$$

Magnetic-Only Result: FAILURE

With $\Gamma_{\text{inv}}^B = 0.007$, the reconstruction error is **143 times larger** than the Cramér-Rao bound. The source location and amplitude are essentially **unrecoverable** from magnetic data alone. This is not a noise problem—even with $100\times$ better SNR, we would only achieve $\Gamma_{\text{inv}}^B = 0.42$.

Step 3: Multi-Physics (B+T) Reconstruction

Thermal condition number (slower $1/r$ decay):

$$\kappa(G_T) = 280 \quad \text{(much better than magnetic)} \tag{11.135}$$

Combined condition number (from Theorem 11.1):

$$\kappa(G_{\text{multi}}) = 195 \quad \text{(actual, via SVD)} \tag{11.136}$$

Verify against theorem bound:

$$\kappa_{\text{bound}} = \frac{1200 \times 280}{\sqrt{1200^2 + 280^2}} = \frac{336000}{1232} = 273 \quad \checkmark \; (\kappa_{\text{multi}} < \kappa_{\text{bound}}) \tag{11.137}$$

Effective SNR for multi-physics (using thermal dominance):

$$\text{SNR}_{\text{eff}} \approx \sqrt{\text{SNR}_B^2 + \text{SNR}_T^2} = \sqrt{8.6^2 + 68^2} = 68.5 \tag{11.138}$$

Multi-physics reconstruction fidelity:

$$\Gamma_{\text{inv}}^{B+T} = \frac{1}{1 + 195/68.5} = \frac{1}{3.85} = \boxed{0.26} \tag{11.139}$$

Step 4: Optimized Multi-Physics with SNR Balancing

Current SNR ratio: $68/8.6 = 7.9$ (thermal dominates)
To balance, increase magnetic integration time by $7.9^2 \approx 62\times$:

- Magnetic: 62 s integration $\rightarrow \text{SNR}_B' = 8.6 \times \sqrt{62} = 68$

- Thermal: 1 s integration $\rightarrow \text{SNR}_T = 68$

With balanced SNR and reduced effective κ:

$$\kappa_{\text{eff}}^{\text{balanced}} \approx 150 \quad \text{(improved weighting)} \tag{11.140}$$

$$\text{SNR}_{\text{combined}} = \sqrt{68^2 + 68^2} = 96 \tag{11.141}$$

$$\Gamma_{\text{inv}}^{\text{optimized}} = \frac{1}{1 + 150/96} = \frac{1}{2.56} = \boxed{0.39} \tag{11.142}$$

Summary of Results:

Configuration	κ	**SNR**	Γ_{inv}
Magnetic only (1 s)	1200	8.6	0.007
Thermal only (1 s)	280	68	0.20
B+T unbalanced (1 s each)	195	68.5	0.26
B+T optimized (62 s B, 1 s T)	150	96	**0.39**

Key Conclusions:

1. Magnetic-only reconstruction **fails completely** ($\Gamma_{\text{inv}} < 0.01$) at this depth

2. Multi-physics improves Γ_{inv} by **37×** ($0.007 \rightarrow 0.26$)

3. SNR optimization provides additional **1.5×** improvement

4. Even optimized, $\Gamma_{\text{inv}} = 0.39$ indicates this depth is at the limit of QFI capability

5. For $\Gamma_{\text{inv}} > 0.9$, maximum depth is approximately $d < 15$ μm with current parameters

Example 11.5: Complete Defect Characterization (I, d, R)

This example demonstrates the **unique capability** of multi-physics measurement: extracting all three defect parameters (I, d, R) from a single measurement, which is **impossible** with any single-physics approach.

Measured Data:

- Magnetic: $B_{\text{peak}} = 320$ nT, $\text{FWHM}_B = 14.0$ μm

- Thermal: $\Delta T_{\text{peak}} = 180$ mK, $\text{FWHM}_T = 24.2$ μm

- Standoff: $z_0 = 5$ μm (known from system calibration)

Step 1: Extract Depth from Magnetic FWHM
For a current-carrying wire, the magnetic field FWHM relates to total distance:

$$\text{FWHM}_B = 2(d + z_0) \quad \Rightarrow \quad d + z_0 = \frac{14.0}{2} = 7.0 \ \mu\text{m} \tag{11.143}$$

$$\boxed{d = 7.0 - 5.0 = 2.0 \ \mu\text{m}} \tag{11.144}$$

Step 2: Verify Depth via Thermal FWHM
For thermal from a line source, $\text{FWHM}_T \approx 2 \times 1.73 \times (d + z_0) = 3.46(d + z_0)$:

$$d + z_0 = \frac{24.2}{3.46} = 7.0 \ \mu\text{m} \quad \checkmark \ (\text{consistent}) \tag{11.145}$$

Additional check—FWHM ratio:

$$\frac{\text{FWHM}_T}{\text{FWHM}_B} = \frac{24.2}{14.0} = 1.73 \approx \sqrt{3} \quad \checkmark \ (\text{confirms point/line source}) \tag{11.146}$$

Step 3: Extract Current from Magnetic Peak
Using the magnetic forward model:

$$B_{\text{peak}} = \frac{\mu_0 I}{2\pi(d + z_0)} \tag{11.147}$$

$$I = \frac{2\pi(d+z_0)B_{\text{peak}}}{\mu_0} = \frac{2\pi \times 7.0 \times 10^{-6} \times 320 \times 10^{-9}}{4\pi \times 10^{-7}} \tag{11.148}$$

$$I = \frac{7.0 \times 320 \times 10^{-15}}{2 \times 10^{-7}} = \frac{2.24 \times 10^{-12}}{2 \times 10^{-7}} = \boxed{11.2 \text{ mA}} \tag{11.149}$$

Step 4: Extract Power from Thermal Peak

Using the thermal forward model:

$$\Delta T_{\text{peak}} = \frac{P}{2\pi k(d+z_0)} \tag{11.150}$$

$$P = 2\pi k(d+z_0)\Delta T_{\text{peak}} = 2\pi \times 150 \times 7.0 \times 10^{-6} \times 0.180 \tag{11.151}$$

$$P = 2\pi \times 150 \times 1.26 \times 10^{-6} = \boxed{1.19 \text{ mW}} \tag{11.152}$$

Step 5: Calculate Resistance

From Joule heating relation $P = I^2 R$:

$$R = \frac{P}{I^2} = \frac{1.19 \times 10^{-3}}{(11.2 \times 10^{-3})^2} = \frac{1.19 \times 10^{-3}}{1.25 \times 10^{-4}} = \boxed{9.5 \text{ } \Omega} \tag{11.153}$$

Step 6: Self-Consistency Verification

The over-determined system allows internal consistency checks:

Check	Expected	Actual
FWHM ratio ($\text{FWHM}_T/\text{FWHM}_B$)	$\sqrt{3} = 1.732$	1.73 ✓
Peak ratio ($k\mu_0 \Delta T/B^2 d$)	$R/(2\pi) = 1.51$	1.48 ✓
Depth from B vs. T	Same	7.0 μm ✓

All consistency checks pass, indicating reliable parameter extraction.

Defect Diagnosis:

Parameter	Value	Interpretation
Depth d	2.0 μm	Metal 2 (M2) layer
Current I	11.2 mA	Moderate current level
Resistance R	9.5 Ω	Elevated (normal via $\sim$1 Ω)
Power P	1.19 mW	Localized hot spot

Diagnosis: The 9.5 Ω resistance (vs. typical 0.5–2 Ω for healthy vias) indicates a **partially voided or high-resistance via** in the M2-M3 interconnect. This defect type would cause reliability issues under electromigration stress.

Key Insight: With magnetic-only measurement, we could determine $I \cdot d$ (the product) but not I and d separately. With thermal-only, we could determine $I^2 R \cdot d$ but not individual parameters. Only the **combination of both** provides the three independent equations needed to solve for three unknowns (I, d, R).

$$\underbrace{B_{\text{peak}}, \text{FWHM}_B}_{\text{2 magnetic observables}} + \underbrace{\Delta T_{\text{peak}}, \text{FWHM}_T}_{\text{2 thermal observables}} \xrightarrow{\text{4 equations}} \underbrace{I, d, R}_{\text{3 unknowns}} + \underbrace{\text{1 consistency check}}_{\text{validation}} \tag{11.154}$$

Example 11.6: False Positive Rejection via Multi-Physics Correlation

A critical challenge in IC failure analysis is distinguishing **real defects** from **measurement artifacts** (noise, environmental interference, ghost images). This example demonstrates how multi-physics correlation provides a powerful discrimination mechanism unavailable to single-physics measurement.

Scenario: A magnetic scan reveals three candidate features:

Feature	B_{peak} (nT)	Location	**Status**
A	450	(x_A, y_A)	Unknown
B	380	(x_B, y_B)	Unknown
C	290	(x_C, y_C)	Unknown

All three features exceed the 5σ detection threshold (5×50 nT $= 250$ nT), so magnetic-only analysis would flag all three as potential defects.

Step 1: Predict Expected Thermal Signatures

If each feature is a real current-carrying defect, the expected thermal signal is:

$$\Delta T_{\text{expected}} = \frac{B_{\text{peak}}^2 \cdot R}{k \mu_0^2} \cdot f(d/z_0) \tag{11.155}$$

For typical defect parameters ($R \approx 10\ \Omega$, $d \approx 10\ \mu$m, $z_0 = 5\ \mu$m):

Feature	B_{peak} (nT)	$\Delta T_{\text{expected}}$ (mK)	SNR_T expected
A	450	85	17
B	380	61	12
C	290	35	7

(Assuming thermal noise floor $\sigma_T = 5$ mK)

Step 2: Measure Thermal at Candidate Locations

Actual thermal measurements at each location:

Feature	$\Delta T_{\text{expected}}$ (mK)	$\Delta T_{\text{measured}}$ (mK)	**Ratio**	**Assessment**
A	85	78	0.92	**CONFIRMED**
B	61	8	0.13	**REJECTED**
C	35	41	1.17	**CONFIRMED**

Step 3: Statistical Analysis

Define the multi-physics correlation metric:

$$\mathcal{R}_{\text{BT}} = \frac{\Delta T_{\text{measured}}}{\Delta T_{\text{expected}}} \tag{11.156}$$

For a real defect: $\mathcal{R}_{\text{BT}} \approx 1.0 \pm 0.3$ (allowing for parameter uncertainty)
For an artifact: $\mathcal{R}_{\text{BT}} \approx 0$ (no physical coupling)
Decision threshold: $\mathcal{R}_{\text{BT}} > 0.5 \Rightarrow$ real defect

Feature	$\mathcal{R}_{\text{BT}}$	**Decision**	**Likely Origin**
A	0.92	Real defect	Current-carrying short
B	0.13	Artifact	Environmental B-field interference
C	1.17	Real defect	Resistive via (slightly higher R)

Step 4: Quantify False Positive Reduction

Single-physics (magnetic only):

- Detection threshold: $B > 250$ nT

- Candidates flagged: 3 (A, B, C)

- Actual defects: 2 (A, C)

- False positive rate: $1/3 = 33\%$

Multi-physics (B+T correlation):

- Detection threshold: $B > 250$ nT AND $\mathcal{R}_{\mathrm{BT}} > 0.5$

- Candidates confirmed: 2 (A, C)

- False positive rate: $0/2 = 0\%$

False positive reduction: $33\% \to 0\%$

Step 5: Physical Explanation of Feature B

Feature B showed strong magnetic signal but negligible thermal correlation. Possible origins:

1. **External interference**: Nearby equipment, power line coupling

2. **Magnetized particle**: Debris on sample surface

3. **Residual magnetization**: Previous measurement artifact

4. **Ghost image**: Optical reflection creating false NV response

All these sources produce magnetic signatures **without associated Joule heating**, hence the thermal null result definitively rules out a current-carrying defect.

Summary—Multi-Physics Discrimination Power:

Metric	Single-Physics	Multi-Physics
False positive rate	33%	<5%
Confirmation confidence	Low	High
Root cause identification	None	Yes
Parameter extraction	$I \cdot d$ only	I, d, R separate

Design Rule 11.8: Multi-Physics Confirmation Protocol

For critical defect calls, require:

$$\mathcal{R}_{\mathrm{BT}} = \frac{\Delta T_{\mathrm{measured}}}{\Delta T_{\mathrm{predicted}}(B_{\mathrm{measured}})} \in [0.5, 2.0] \tag{11.157}$$

We use $\mathcal{R}_{\mathrm{BT}}$ (calligraphic $\mathcal{R}$) for the confirmation ratio to distinguish it from the noise cross-correlation coefficient ρ_{ij} used in Condition C1.

Features outside this range should be flagged for additional investigation (higher $\mathcal{R}_{\mathrm{BT}}$: higher resistance; lower $\mathcal{R}_{\mathrm{BT}}$: artifact).

Connecting Φ_{multi} and $\mathcal{R}_{\text{BT}}$: Two Complementary Multi-Physics Metrics

The chapter employs two distinct multi-physics metrics that serve different roles in the QFI workflow:

	Multi-Physics Factor Φ_{multi}	**Confirmation Ratio $\mathcal{R}_{\text{BT}}$**
Definition	$\Phi_{\text{multi}} = I_{\text{joint}}/\sum_i I_i$ (Fisher information gain)	$\mathcal{R}_{\text{BT}} = \Delta T_{\text{measured}}/\Delta T_{\text{predicted}}(B_{\text{measured}})$
Measures	*Global identifiability*—how much the combined system reduces parameter uncertainty vs. independent channels	*Physical self-consistency*—whether the observed thermal and magnetic signatures are compatible with a single defect model
When to use	*System design*: predicting whether multi-physics will improve Γ_{inv} for a given geometry and noise budget	*Defect diagnosis*: confirming or rejecting a candidate defect after reconstruction
Computed from	Forward model matrices $\mathbf{G}_i$ and noise covariances (before measurement)	Actual measurement data D_B, D_T (after measurement)
Acceptance	$\Phi_{\text{multi}} > 1.5$ (worthwhile to add channel)	$\mathcal{R}_{\text{BT}} \in [0.5, 2.0]$ (consistent with defect hypothesis)

Relationship: $\Phi_{\text{multi}} > 1$ is a *necessary precondition* for $\mathcal{R}_{\text{BT}}$ to carry discriminative power. If $\Phi_{\text{multi}} \approx 1$ (channels degenerate), then $\mathcal{R}_{\text{BT}}$ is dominated by noise and loses its diagnostic value. Conversely, high Φ_{multi} does not guarantee $\mathcal{R}_{\text{BT}} \in [0.5, 2.0]$—the measured data may still indicate an artifact.

11.11 Chapter Summary

This chapter developed the theoretical foundation for multi-physics forward models in QFI, establishing that combining multiple physics channels fundamentally improves the conditioning of the inverse problem. The central result—Theorem 11.1 (Multi-Physics Conditioning)—proves that $\kappa(\mathbf{G}_{\text{multi}}) < \kappa(\mathbf{G}_{\text{single}})$ when conditions C1–C4 are satisfied, directly improving reconstruction fidelity Γ_{inv}.

11.11.1 Key Results

The chapter established the following principal results:

1. **Thermal Forward Model** (Sections 11.2–11.3): Derived $\mathbf{G}_T$ from the steady-state heat equation with Joule heating source $Q = I^2 R$. The thermal field exhibits different spatial decay ($\sim 1/r$) compared to magnetic ($\sim 1/r^2$), providing complementary depth information.

2. **Thermoelastic Coupling** (Section 11.4): Established the strain forward model $\mathbf{G}_\varepsilon$ through thermal expansion coefficient α. The linear chain $I \to T \to \varepsilon$ provides a third independent observation channel.

3. **Combined Forward Model** (Section 11.5): Constructed the stacked multi-physics forward model:

$$\mathbf{G}_{\text{multi}} = \begin{bmatrix} \mathbf{G}_B \\ \mathbf{G}_T \\ \mathbf{G}_\varepsilon \end{bmatrix} \tag{11.158}$$

with demonstrated rank increase from N (single-physics) to up to $3N$ (three-channel multi-physics).

4. **Conditioning Theorem** (Section 11.6): Proved Theorem 11.1 showing that the combined forward model has strictly better conditioning than any individual channel:

$$\kappa(\mathbf{G}_{\text{multi}}) \leq \frac{\kappa(\mathbf{G}_B) \cdot \kappa(\mathbf{G}_T)}{\sqrt{\kappa(\mathbf{G}_B)^2 + \kappa(\mathbf{G}_T)^2}} \tag{11.159}$$

with equality only when the column spaces are orthogonal.

5. **Conditions for Improvement** (Section 11.7): Identified four necessary conditions (C1–C4) for the conditioning theorem to provide practical benefit:

   - **C1 (Independence)**: Noise in channel i uncorrelated with channel j ($\rho_{ij} < 0.1$)
   - **C2 (Non-degeneracy)**: Forward models not proportional ($\theta_{ij} > 30°$)
   - **C3 (SNR balance)**: SNR ratio within $10\times$ across channels
   - **C4 (Temporal stability)**: Drift $<$ noise floor during acquisition

6. **Failure Mode Analysis** (Section 11.8): Characterized four distinct failure modes when C1–C4 are violated, with detection methods and mitigation strategies. Key insight: violation of any single condition reduces $\Phi_{\text{multi}} \to 1$, eliminating the multi-physics advantage.

7. **Quantitative Predictions** (Section 11.9): Established numerical predictions for typical IC inspection geometries:

   - Condition number improvement: $\kappa_{\text{multi}} \approx (2\text{–}4)\times$ better than κ_B
   - Multi-physics factor: $\Phi_{\text{multi}} = 2\text{–}4$ for typical defects
   - Depth extension: $1.5\text{–}2\times$ deeper recoverable sources
   - SNR requirement reduction: $2\text{–}5\times$ lower SNR for equivalent Γ_{inv}

11.11.2   Worked Examples Summary

Three worked examples demonstrated the practical application of multi-physics forward models:

Table 11.15: Chapter 11 worked examples summary.

Example	Title	Key Result	Section
11.10.1	TSV Defect Analysis	$\Phi_{\text{multi}} = 2.75$ for B+T+ε; depth accuracy $\pm 0.5\,\mu$m vs. $\pm 3\,\mu$m (B-only)	11.10.1
11.10.2	Condition Number Verification	$\kappa_{\text{multi}} = 127$ vs. $\kappa_B = 892$ ($7\times$ improvement) at $z_0 = 15\,\mu$m	11.10.2
11.10.3	C1–C4 Failure Diagnosis	Identified C2 violation ($\theta = 12°$) causing $\Phi_{\text{multi}} = 1.1$ despite dual-channel	11.10.3

11.11.3 Design Rules from This Chapter

Table 11.16: Chapter 11 design rules summary.

Rule	Statement	Quantitative Criterion
DR 11.1	Multi-physics achieves superior Γ_{inv} for typical IC geometries	$\Gamma_{\text{inv}} > 0.9$ with B+T vs. $\Gamma_{\text{inv}} < 0.7$ (B-only) for $z > 2h$
DR 11.2	Noise independence (C1) is prerequisite for $\Phi_{\text{multi}} > 1$	Cross-correlation $\mathcal{R}_{\text{BT}} < 0.1$ required
DR 11.3	Non-degeneracy (C2) requires distinct decay profiles	Principal angle $\theta > 30°$ between column spaces
DR 11.4	SNR balance (C3) prevents single-channel dominance	$\text{SNR}_{\text{max}}/\text{SNR}_{\text{min}} < 10$ across channels
DR 11.5	Temporal stability (C4) avoids Γ_{mm} collapse	Drift rate $<$ noise floor during acquisition sequence
DR 11.6	Thermal channel timing must account for diffusion	$\tau_{\text{thermal}} = L^2/(4D) \approx 1\text{–}10\ \mu\text{s}$ for IC scales
DR 11.7	Multi-physics extends recoverable depth by $\sqrt{2}$	$z_{\text{max,multi}} \approx \sqrt{2}\text{–}1.5 \times z_{\text{max,single}}$ ($\sqrt{2}$ for two-channel; up to 1.5 for three-channel with optimized weighting)

11.11.4 Equations to Remember

Table 11.17: Key equations from Chapter 11.

Equation	Name	Reference
$\nabla^2 T = -Q/k,\ Q = I^2 R$	Thermal forward model	Eq. (11.3)
$\varepsilon = \alpha \cdot \Delta T$	Thermoelastic coupling	Eq. (11.8)
$\mathbf{G}_{\text{multi}} = [\mathbf{G}_B; \mathbf{G}_T; \mathbf{G}_\varepsilon]$	Combined forward model	Eq. (11.12)
$\kappa_{\text{multi}} \leq \kappa_B \kappa_T / \sqrt{\kappa_B^2 + \kappa_T^2}$	Conditioning theorem	Eq. (11.18)
$\Phi_{\text{multi}} = I_{\text{joint}} / \sum_i I_i$	Multi-physics factor	Eq. (11.24)
$\Gamma_{\text{inv}} \approx 1/(1 + \kappa/\text{SNR})$	Reconstruction fidelity proxy (amplitude-domain)	Eq. (11.31)

11.11.5 Figure Summary

Table 11.18: Chapter 11 figure summary with key insights.

Figure	Title	Key Insight
11.1	Chapter Roadmap	Multi-physics forward model construction pipeline
11.2	Decay Comparison	Thermal ($\sim 1/r$) vs. magnetic ($\sim 1/r^2$) provides complementary depth sensitivity
11.3	Matrix Structure	$\mathbf{G}_{\mathrm{multi}}$ SVD shows rank increase and improved singular value distribution
11.4	Conditioning Analysis	Theorem 11.1 verification: $\kappa_{\mathrm{multi}} < \min(\kappa_B, \kappa_T)$ for all depth/standoff ratios
11.5	Conditions Summary	Visual C1–C4 decision tree for multi-physics benefit assessment
11.6	Failure Modes	Four-panel analysis showing $\Phi_{\mathrm{multi}} \to 1$ under each violation type
11.7	Γ_{inv} Predictions	Quantitative improvement factors across parameter space

11.11.6 Connection to QFI Framework

Chapter 11 addresses the forward model operator $\mathcal{G}$ in the QFI operator stack:

$$S \xrightarrow{\mathcal{G}} F \xrightarrow{\mathcal{M}} D \xrightarrow{\mathcal{R}} \hat{S} \tag{11.160}$$

The multi-physics forward model $\mathbf{G}_{\mathrm{multi}}$ directly impacts two components of the Q_{IFOM}:

1. **Reconstruction Fidelity** Γ_{inv}: Improved conditioning ($\kappa_{\mathrm{multi}} < \kappa_{\mathrm{single}}$) directly increases Γ_{inv} through the proxy relationship:

$$\Gamma_{\mathrm{inv}} \propto \frac{1}{1 + (\kappa/\kappa_0)^2/\mathrm{SNR}^2} \tag{11.161}$$

2. **Multi-Physics Factor** Φ_{multi}: Independent physics channels provide additional Fisher information:

$$\mathbf{J}_{\mathrm{multi}} = \mathbf{J}_B + \mathbf{J}_T + \mathbf{J}_\varepsilon > \mathbf{J}_{\mathrm{single}} \tag{11.162}$$

when C1–C4 are satisfied.

The combined effect on Q_{IFOM} is multiplicative:

$$Q_{\mathrm{IFOM,multi}} = Q_{\mathrm{FOM}} \times \Gamma_{\mathrm{inv}}^{(\mathrm{multi})} \times \Gamma_{\mathrm{mm}} \tag{11.163}$$

where typically $\Gamma_{\mathrm{inv}}^{(\mathrm{multi})}/\Gamma_{\mathrm{inv}}^{(\mathrm{single})} = 1.2$–$3\times$ for sources at depth $z > 2h$.

11.11.7 Looking Forward

This chapter established the theoretical foundation for multi-physics advantage. Subsequent chapters build on these results:

- **Chapter 12 (System Architecture)**: Implements practical multi-physics measurement sequences that satisfy C1–C4 in hardware

- **Chapter 13 (Standoff and Depth)**: Applies the extended depth capability ($z_{\mathrm{max,multi}} > z_{\mathrm{max,single}}$) to practical inspection geometries

- **Chapter 14 (Reconstruction Algorithms)**: Develops reconstruction algorithms $\mathcal{R}$ optimized for the improved conditioning of $\mathbf{G}_{\mathrm{multi}}$

- **Chapter 15 (Current Density Reconstruction)**: Applies multi-physics forward models to the specific case of $\mathbf{J}(\mathbf{r})$ reconstruction in semiconductor FA

11.11.8 Chapter Takeaways

Multi-Physics Conditioning Advantage

The central insight of this chapter:

$$\boxed{\kappa(\mathbf{G}_{\mathrm{multi}}) < \kappa(\mathbf{G}_{\mathrm{single}}) \implies \Gamma_{\mathrm{inv}}^{(\mathrm{multi})} > \Gamma_{\mathrm{inv}}^{(\mathrm{single})}} \qquad (11.164)$$

Multi-physics measurement fundamentally improves reconstruction fidelity by reducing forward model conditioning. This is not merely additive information—it is multiplicative improvement in the solvability of the inverse problem.

Three things to remember from Chapter 11:

1. **Different decay = depth disambiguation**: Thermal ($1/r$) and magnetic ($1/r^2$) fields have different depth sensitivities, breaking the depth-amplitude degeneracy that limits single-physics QFI.

2. **Conditions matter**: The multi-physics advantage requires C1–C4 to be satisfied. Verify these conditions *before* claiming $\Phi_{\mathrm{multi}} > 1$.

3. **Quantitative improvement**: For typical IC inspection at $z = 2$–$4 \times h$ (standoff), expect κ reduction of 2–4$\times$ and Γ_{inv} improvement of 1.2–3$\times$ with B+T dual-channel measurement.

Problems and Solution Hints

Problem 11.1: Layered Media Green's Function

Derive the thermal Green's function for a three-layer system: silicon ($k_1 = 150$ W/(m·K), thickness $h_1 = 300$ μm), SiO$_2$ interlayer ($k_2 = 1.4$ W/(m·K), thickness $h_2 = 2$ μm), and diamond ($k_3 = 2000$ W/(m·K), semi-infinite). A point source is located at depth $d = 10$ μm in the silicon.

    (a) Set up the image series for each interface.
    (b) Compute the first 5 image contributions.
    (c) Compare surface temperature to the homogeneous silicon case.
    Hint: The thermal reflection coefficient at interface i-$(i+1)$ is $r_i = (k_{i+1} - k_i)/(k_{i+1} + k_i)$. The SiO$_2$ layer acts as a thermal barrier, significantly affecting heat flow.

Problem 11.2: Optimal Channel Weighting

For a two-channel system with unequal noise variances σ_1^2 and σ_2^2, derive the optimal weighting matrix $\mathbf{W}$ that minimizes the trace of the posterior covariance in Bayesian reconstruction.

    (a) Write the weighted least-squares objective function.
    (b) Show that optimal weights are $w_i \propto 1/\sigma_i^2$.
    (c) Derive the effective condition number for the weighted system.
    Hint: The Fisher Information Matrix for weighted observations is $\mathbf{J} = \mathbf{G}^T \mathbf{W} \mathbf{G}$ where $\mathbf{W} = \mathrm{diag}(1/\sigma_i^2)$.

Problem 11.3: Principal Angle Computation

For forward models $\mathbf{G}_B$ and $\mathbf{G}_T$ constructed from a 16×16 measurement grid with sources at depth d:

    (a) Compute the principal angles as a function of depth for $d \in [2, 50]$ μm.
    (b) Identify the depth at which $\theta_{\min} = 30°$ (C2 threshold).
    (c) Explain physically why principal angles change with depth.
    Hint: Use the SVD to find left singular vectors $\mathbf{U}_B$ and $\mathbf{U}_T$, then compute singular values of $\mathbf{U}_B^T \mathbf{U}_T$.

Problem 11.4: AC Thermal Measurement

When current is modulated at frequency f, the thermal response is attenuated and phase-shifted due to thermal diffusion.

    (a) Derive the frequency-dependent thermal transfer function $H_T(f)$ for a point source at depth d.
    (b) Show that $|H_T(f)| \propto 1/\sqrt{f}$ at high frequency.
    (c) Design a multi-frequency measurement protocol that provides additional depth information beyond DC measurement.
    Hint: The thermal diffusion length is $L_{\mathrm{th}} = \sqrt{2\alpha_{\mathrm{th}}/(2\pi f)}$. When $L_{\mathrm{th}} < d$, the surface thermal signal is attenuated.

Problem 11.5: Strain Channel Independence

Under what conditions does the strain channel G_ε provide information independent of the thermal channel G_T?

    (a) Derive the relationship $G_\varepsilon = \alpha_{\mathrm{CTE}} \cdot G_T$ for unconstrained thermal expansion.
    (b) Model a constrained structure (fixed boundaries) and show that $G_\varepsilon \neq \alpha G_T$ in general.
    (c) Compute the principal angle between G_T and G_ε for a flip-chip geometry with die attach.

Hint: Mechanical constraints introduce stress that depends on the distance to boundaries, not just local temperature.

References

[1] H. S. Carslaw and J. C. Jaeger, *Conduction of Heat in Solids*, 2nd ed. Oxford: Clarendon Press, 1959.

[2] F. Dolde *et al.*, "Electric-field sensing using single diamond spins," *Nat. Phys.*, vol. 7, pp. 459–463, 2011.

[3] P. Neumann *et al.*, "High-precision nanoscale temperature sensing using single defects in diamond," *Nano Lett.*, vol. 13, pp. 2738–2742, 2013.

[4] G. Kucsko *et al.*, "Nanometre-scale thermometry in a living cell," *Nature*, vol. 500, pp. 54–58, 2013.

[5] D. A. Broadway *et al.*, "Microscopic imaging of the stress tensor in diamond using in situ quantum sensors," *Nano Lett.*, vol. 19, pp. 4543–4550, 2019.

[6] M. W. Doherty *et al.*, "The nitrogen-vacancy colour centre in diamond," *Phys. Rep.*, vol. 528, pp. 1–45, 2013.

[7] A. Tarantola, *Inverse Problem Theory and Methods for Model Parameter Estimation*. Philadelphia: SIAM, 2005.

[8] J. Kaipio and E. Somersalo, *Statistical and Computational Inverse Problems*. New York: Springer, 2005.

[9] C. R. Vogel, *Computational Methods for Inverse Problems*. Philadelphia: SIAM, 2002.

[10] G. H. Golub and C. F. Van Loan, *Matrix Computations*, 4th ed. Baltimore: Johns Hopkins University Press, 2013.

[11] L. R. Lines, A. K. Schultz, and S. Treitel, "Cooperative inversion of geophysical data," *Geophysics*, vol. 53, pp. 8–20, 1988.

[12] K. Vozoff and D. L. B. Jupp, "Joint inversion of geophysical data," *Geophys. J. R. Astron. Soc.*, vol. 42, pp. 977–991, 1975.

[13] T. Wolf *et al.*, "Subpicotesla diamond magnetometry," *Phys. Rev. X*, vol. 5, 041001, 2015.

[14] P. Kehayias *et al.*, "Imaging crystal stress in diamond using ensembles of nitrogen-vacancy centers," *Phys. Rev. B*, vol. 100, 174103, 2019.

[15] M. Fujiwara *et al.*, "Real-time nanodiamond thermometry probing in vivo thermogenic responses," *Sci. Adv.*, vol. 6, eaba9636, 2020.